Chapter 10
Applications of Underwater Shock Wave Research to Medicine

10.1 Extracorporeal Shock Wave Lithotripsy (ESWL)

In 1981, Professor M. Kuwahara of the Department of Urology, School of Medicine, Tohoku University invited us to develop a prototype lithotripter using micro explosions. Then the collaboration started applying results of the basic experiments to design a lithotripsy for clinical use.

A shock wave application to medicine was initiated by Yutkin (1950). He, for the first time, used electrical discharges to non-invasively remove urinary tract stones by insertion of a thin electrode through a urethra into a urinary bladder. Touching the electrode on urinary tract stones, he cracked the stones by the exposure of spark generated high-pressures. Later, fragments of the stones were removed using forceps.

Urologists in the world followed his novel technique. Various devices were developed and successfully applied to clinical treatments. A history of development of lithotripters are summarized in Loske (2007). Chaussey et al. (1986) commented that a basic idea of a lithotripsy was initiated by Heustler. His shock wave research was supervised by Professor Schardin who was a director of Ernst Mach Institute and was one of the students of Ernst Mach (Krehl 2009). The German tradition of the shock wave research was extended to this medical application.

An underwater shock wave generated by micro-explosion has a very high over-pressure but its Mach number is very close unity and behaves like a sound wave. The underwater shock wave generated at a focal point inside a truncated ellipsoidal reflector is focused at another focal point outside the reflector. As human bodies have slightly inhomogeneous structures but their acoustic impedances are more or less similar to that in water. Therefore, underwater shock waves generated at a focal point outside human bodies could focus on a kidney stone inside a human body. The pressures focused was high enough to disintegrate the kidney stone. Heustler developed his lithotripter based on this principle and the Dornier Systems succeeded his ideal and constructed the prototype lithotripter.

© Springer Nature Switzerland AG 2019

K. Takayama, *Visualization of Shock Wave Phenomena*,
https://doi.org/10.1007/978-3-030-19451-2_10

Chaussey et al. (1986) named this lithotripsy as extracorporeal shock wave lithotripsy (ESWL). 4–5% of people in the world are estimated to suffer urinary tract stone disease and then it would be wonderful to cure millions of people by applying with this non-invasive lithotripsy. Chaussey et al. (1982) used electric discharges for producing underwater shock waves. Kambe et al. (1986) generated underwater shock waves by detonating small PbN_6 pellets in a controlled way and proved that this method was suited for medical applications.

10.2 Truncated Ellipsoidal Reflector

Figure 10.1 shows visualizations of shock wave focusing and its numerical pressure distribution. A shock wave was generated at a focal point inside a truncated ellipsoidal reflector of minor radius of 45 mm × major radius of 63.6 mm made of acryl. The direct wave was released from the focal point and diverging, whereas the reflected shock wave propagates toward the second focal point outside the reflector. In the second picture, the reflected shock wave focused at the second focal point outside the reflector. A very sharp accumulation of pressures was observed at the second focal point (Obara 2001).

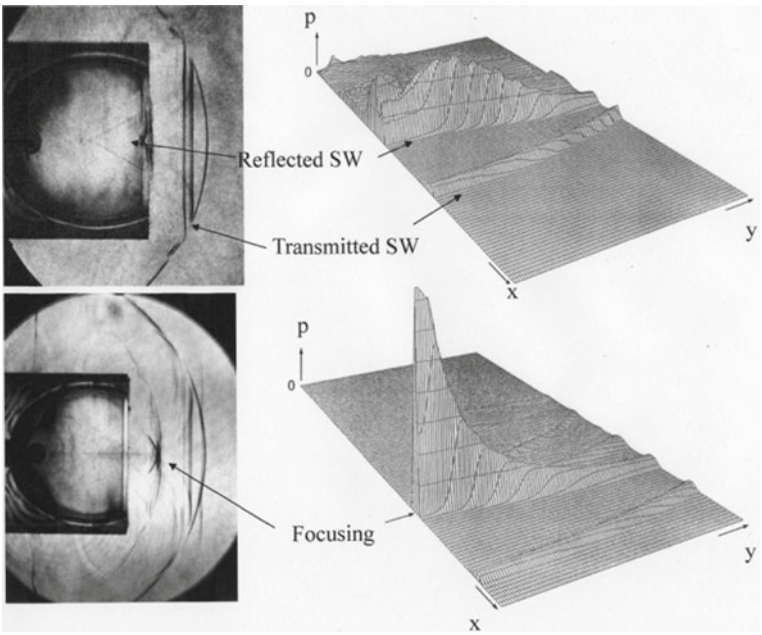

Fig. 10.1 Shock wave focusing using a truncated ellipsoidal reflector made of acryl and numerical simulation pressure distribution in x, y-plane (Obara 2001)

Prototype reflectors were larger than this test model but their character was almost the same as that of the test model. The prototype reflectors generated a maximal pressure at about 100 MPa but the test model generated 50 MPa which decreased to ambient pressure in a few μs. The half width of pressure profiles had approximately from 2.0 to 4.0 mm. High pressures at a focal point inside human bodies damage, at the same time, tissues. Therefore, the value of peak pressures and the pressure profile should be optimized hopefully to minimize the tissue damage. Kidney stones were disintegrated not by a single shock wave focusing. The shock waves were repeated focused and stones were gradually disintegrated. On the stone exposed to shock wave focusing, at first compression stress waves propagated inside the stone and the reflected stress wave from its rear surface became a tensile stress wave. Then the transmitted compression stress wave and the tensile stress wave combined and effectively crashed the stone. The stone was, therefore, disintegrated at its frontal side and at its rear side as well. Hence to maximize the value of the compression stress wave and the tensile stress wave, Chaussey et al. (1986) pointed out that the half width of the peak focusing pressure profile should have the length of about one half to one third of the stone diameter. The shape of the prototype reflector was optimized following his empirical observation.

In Fig. 10.2, eight half-truncated ellipsoidal reflectors were examined in which the major radii were varied while the minor radius was fixed to be 45 mm. The parameter e denotes the focal length from the exit, and the value ranges from 30 to 78 mm. f is the f-number of the reflector, a ratio of the focal distance to the diameter of the opening 90 mm. The value ranges from 0.33 to 0.87. A 10 mg PbN_6 pellet placed at the first focal point inside reflectors was detonated. The peak pressures were measured along the axis. Figure 10.3 summarize the results.

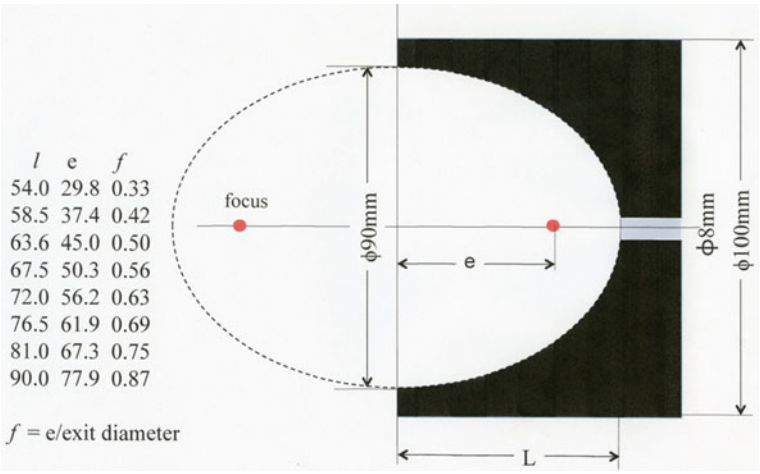

Fig. 10.2 Geometry of present half truncated reflector: minor radius = 45 mm. Major radius *l* variable from 54 mm to 90 mm (Obara 2001)

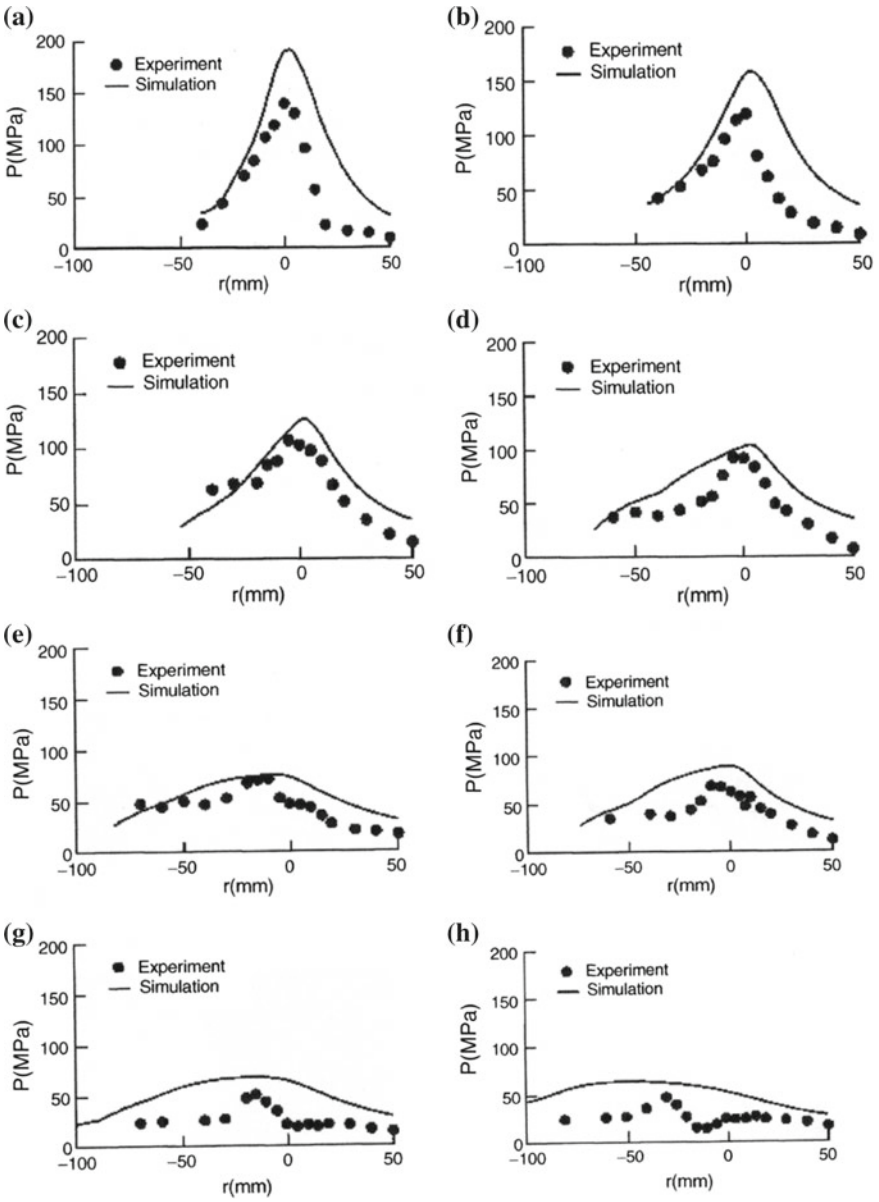

Fig. 10.3 Pressure profiles of reflectors presented in Fig. 10.2: **a** f = 0.33, L = 54.0 mm; **b** f = 0.42, L = 58.5 mm; **c** f = 0.50, L = 63.6 mm; **d** f = 0.56, L = 67.5 mm; **e** f = 0.63, L = 72.0 mm; **f** f = 0.69, L = 76.5 mm; **g** f = 0.75, L = 81.0 mm; **h** f = 0.87, L = 90.0 mm (Chaussey et al. 1986)

Figure 10.3 show peak pressure distributions along the major axis shown in Fig. 10.2 and the results of numerical simulations. The maximal peak pressure in Fig. 10.2a is approximately 160 MPa. This value is too high to safely apply to clinical treatments. Favorable pressures applicable to the ESWL in vivo is about 20–30 MPa, since the kidney stone's maximal yielding stress is at most 80 kg/cm^2 (Chaussey 1983). The peak pressure attenuates inside human bodies is about at the factor of 1/4 to 1/2. Hence, by taking these effects into account, the peak pressure focused at the second focal point should range in vivo from 60 to 100 MPa. The reflector shown in Fig. 10.3b, generates the peak pressure of approximately 140 MPa and the corresponding numerical result agrees well with the measured value. In the case of reflectors with larger f-numbers, the peak pressure so far generated is low and their focal point are slightly deviated from the exact second focal point. Expansion waves created at the reflectors' opening also converged at the second focal point. In the reflectors having large f-number, the procedure of focusing interacted with converging expansion waves and then the maximal peak pressure appeared in the position ahead of the second focal point. The slight deviation of the position at which the peak pressure appeared in the measurement and numerical simulation was attributable to the presence of detonation product gas, the so-called fire ball. In the experiments, the reflected shock wave interacted with the fire ball but this effect is neglected in the numerical simulations.

10.2.1 Prototype Ellipsoidal Reflector

Reflectors having larger f-number and longer stand-off distances may have been useful shape for clinical treatments, however, as seen in Fig. 10.3e–h, their peak pressures are about 50 MPa and their focal points are deviated toward the reflectors' openings. In conclusion, the reflectors are not suited for clinical use. The reflectors with a small f-number as seen in Fig. 10.3a, b, generate high peak pressure which will readily damage tissues. Hence, reflectors having shapes seen in Fig. 10.2c, d are appropriate.

Taking physical features of average Japanese adults into consideration, kidneys are positioned at about 100 mm from body surfaces. Hence, the distance from the reflector's opening to kidney ranges from at least 130–140 mm and the reflector's f-number is about 0.5.

Prototype reflectors of different configurations were made of brass and their pressure profiles were measured. Lastly, the #2 prototype reflector of f = 0.5 with the minor diameter of approximately 180 mm is manufactured. A 10 mg PbN_6 pellet was attached on the edge of 0.6 mm core diameter optical fiber and positioned at the first focal point inside the #2 reflector. Transmissions of a Q-switched Nd:YAG laser beam through the optical fiber ignited the pellet. Pressures were measured along the major axis with a pressure transducer, Kistler model 601H and PVDF (poly vinyl denefluoride) pressure transducers which were made of a 5 mm diameter sheet of polyvinyldene difluoride and manufactured in house.

The pressure distribution is shown in Fig. 10.4. The ordinate denotes the peak pressure in MPa and the abscissa denotes the axial distance in mm. The origin is the second focal point. The shock wave propagates to the left. The maximal peak pressure is about 85 MPa, which is high enough to safely disintegrate kidney stones. The maximal peak pressures appear at about 5 mm toward the focal point. The similar trend was also observed in model reflectors as seen in Fig. 10.2. The deviation of the position at which the peak pressure appeared was attributable to the interaction of the reflected shock wave with the fire ball.

In Fig. 10.5, double exposure and single exposure interferograms show the disintegration of a 10 mm diameter sintered alumina sphere placed at the secondary focal point of #2 reflector. The shock wave propagated from right to left. Upon the shock wave focusing on the alumina sphere, the pressure on the reflector side was so enhanced that fringes appeared densely on the stone model in Fig. 10.5a, b. In these double exposure interferograms, the shadow of the alumina sphere before and after the shock wave focusing were superimposed so that the shape of deformed sphere looked disturbed. The grey shadows visible downstream of the sphere were a bubble cloud. Figure 10.5c is a single exposure interferogram taken at 20 μs after the time instant when Fig. 10.5b was taken. On the frontal side of the sphere, a bubble cloud appeared and the alumina sphere was slightly deformed. Figure 10.4

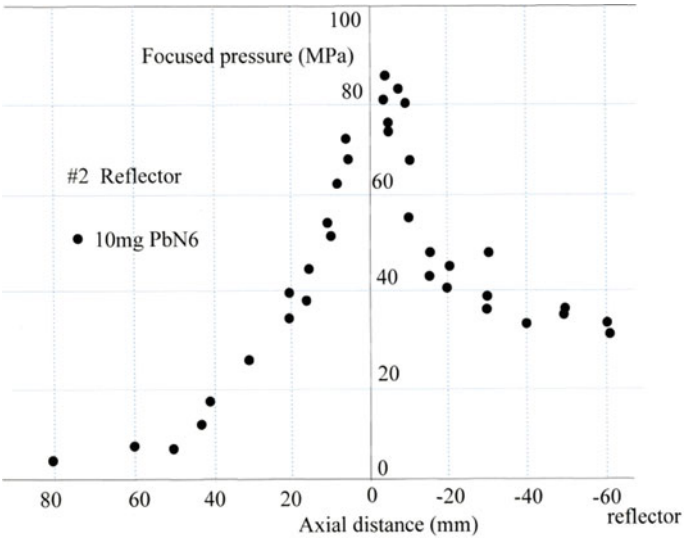

Fig. 10.4 Measured pressure profile of #2 reflector (Obara 2001)

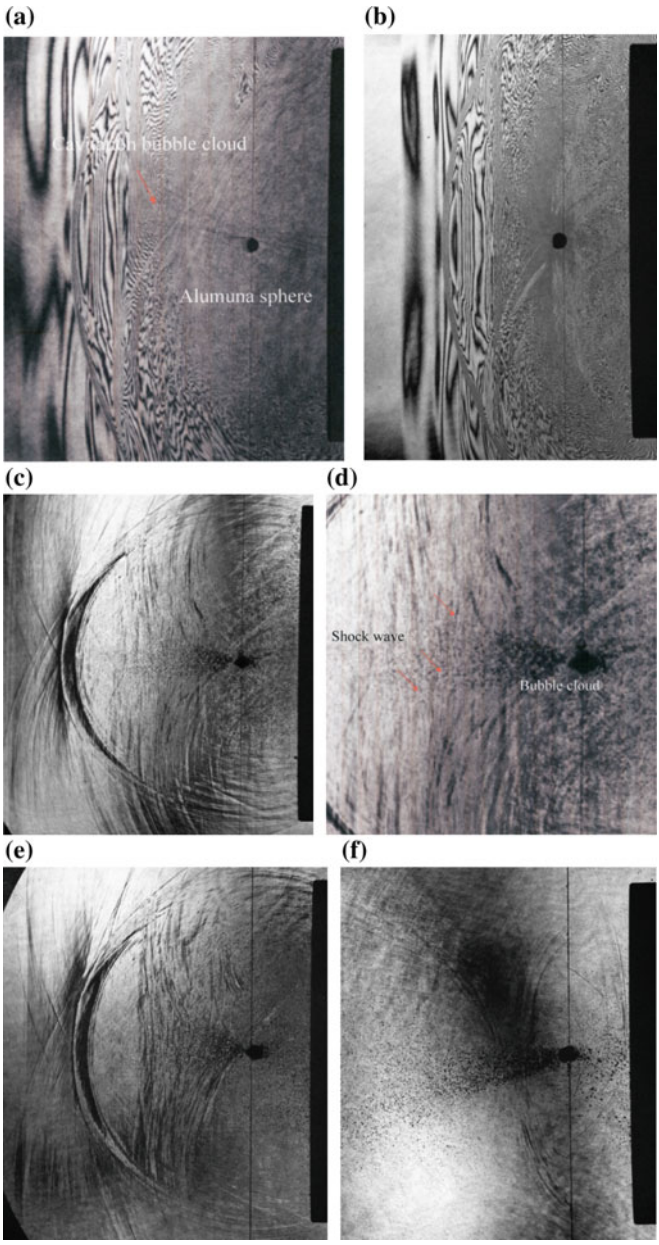

Fig. 10.5 Sintered 10 mm outer diameter alumina, focusing by ellipsoidal reflector, at 1013 hPa, 286.7 K: **a** #83122201, 90 μs, Shock waves are generated by exploding 9.1 mg PbN_6 pellet; **b** #83122202, 80 μs from trigger point, 9.1 mg PbN_6 pellet; **c** #83122203, 100 μs 7.9 mg PbN_6, single exposure; **d** Enlargement of (**c**); **e** #83122204, 140 μs, 7.7 mg PbN_6, single exposure; **f** #83122205, 249 μs, 7.5 mg, PbN_6, single exposure; **g** Enlargement of (**f**); **h** #83122206, 400 μs, 7.1 mg, PbN_6; **i** #83122210, 850 μs, 5.8 mg, PbN_6, single exposure; **j** #83122303, 1200 μs, 9.3 mg, PbN_6, single exposure; **k** #83122306, 2500 μs, 8.7 mg, PbN_6, single exposure

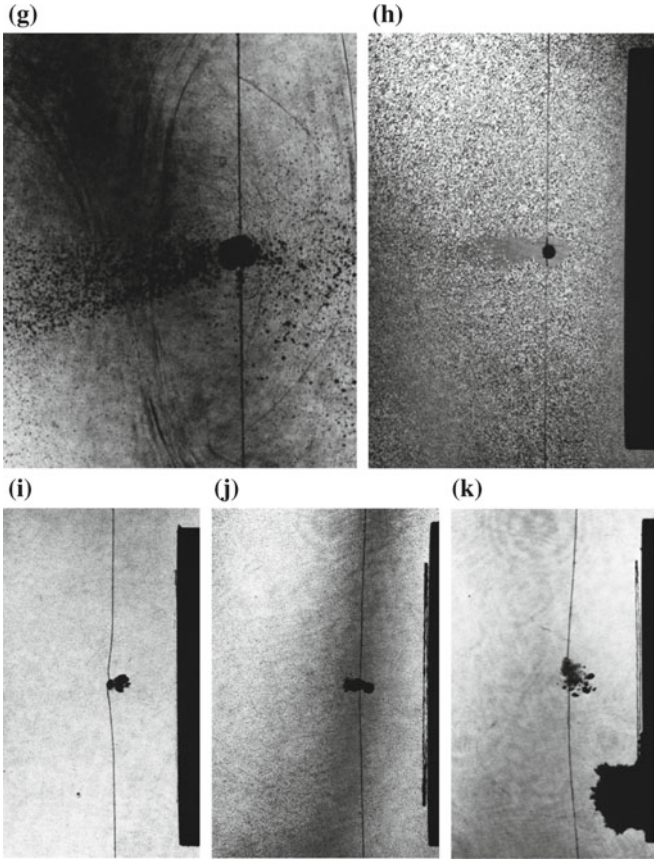

Fig. 10.5 (continued)

showed the higher peak pressure in the frontal side but decreasing pressure on the rear side. Hence this pressure gradient promoted the generation of cavitation bubble cloud which were shattered toward the downstream. Figure 10.5d is an enlarged image of Fig. 10.5c. Small rings observed at the tail of the cavitation cloud, which were secondary shock waves generated at the collapsing cavitation bubbles. Bubbles were spatially and temporally randomly collapsed responding to pressure fluctuations.

The distribution of cavitation bubbles is readily identified by observation of single exposure interferograms but the double exposure interferograms recorded all the changes in phase angles during the double exposure including subtle and major density variations, whereas the single exposure one could record only major density changes. Figure 10.5c–f are single exposure pictures and their enlargements.

In Fig. 10.5d, g ring shaped patterns are secondary shock waves occurring at bubbles collapse. It should be noticed that all the bubbles are not collapsed but only a selective number of bubbles collapsed.

Figure 10.5i–k show later stages. The alumina sphere was disintegrated. The fire ball contained lead vapor which was heavier than water. Therefore, long time after explosion, the fire ball came out along the reflector's lower wall as seen in Fig. 10.5k.

10.2.2 Preparatory Tests

Prior to the application of the prototype reflector to in vitro experiments, the shock wave mitigation through tissues was investigated. The shock wave attenuation through a slice of a swine meat of 15 mm × 100 mm, and 10 mm in thickness suspended at the exit of truncated reflector was observed as shown in Fig. 10.6.

Figure 10.7 show shock wave interactions with a ceramic sphere, a lib cartilage, and a rubber balloon containing swine liver. Shock waves propagated faster in the ceramic sphere and slightly faster over rubber balloons.

Figures 10.8 and 10.9 show shock wave interaction with extracted kidney stones. Depending on the type of kidney stones, interaction patterns differ from each other.

Figure 10.10 show sequential observations of shock wave focusing using the #2 reflector and the effect of sponge layer placed in front of the reflector opening. In Fig. 10.10a–c, the concentration of fringes at the second focal point are shown. Although the sponge sheet covered lower half of the opening, still the focusing was achieved. Figure 10.10d–g shows the procedure of focusing.

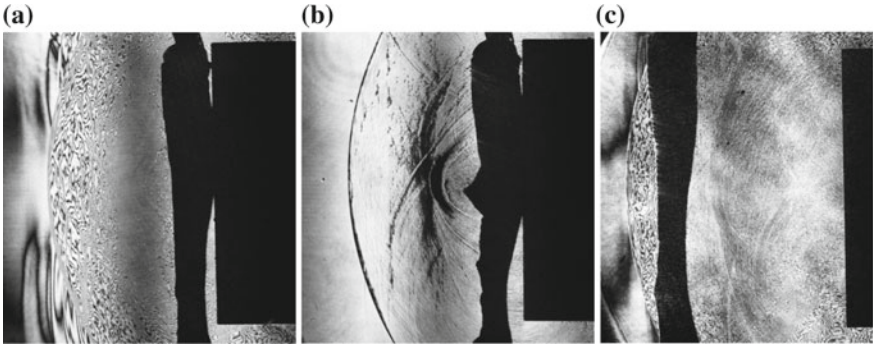

Fig. 10.6 Effects of a swine meat of 15 mm × 100 mm, thickness 10 mm on shock wave focusing: **a** #84030506, 31 μs from trigger point, 11.0 mg PbN_6; **b** #84030505, 31 μs, 11.8 mg PbN_6 single exposure; **c** #84030510, 39 μs, 9.0 mg PbN_6

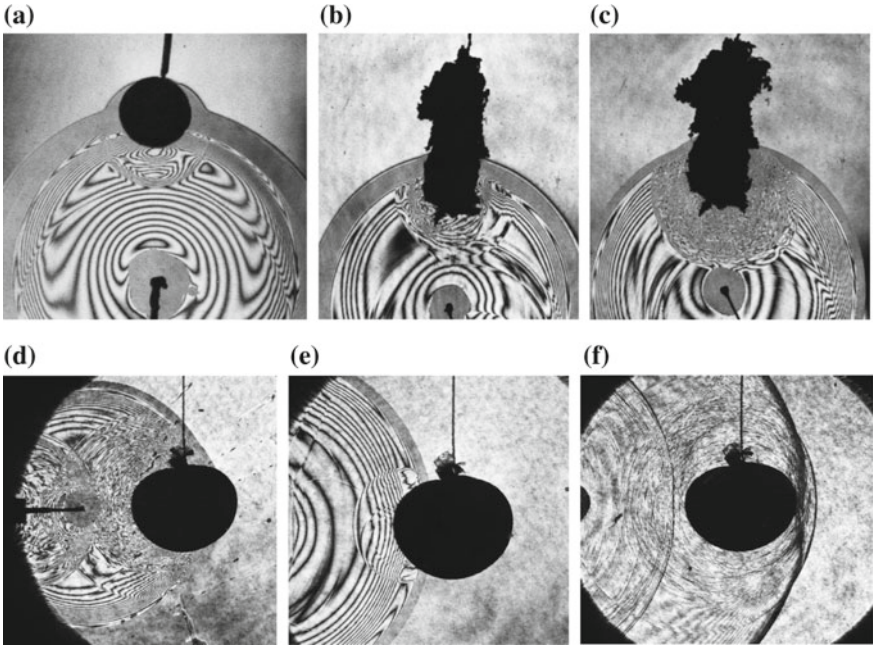

Fig. 10.7 Shock wave interaction with ceramic sphere and cartilage: **a** #84052105, 10 mm diameter ceramic sphere, AgN_3 11 mg; **b** #84051607, rib cartilage, 10 mg AgN_3; **c** #84051608, rib cartilage, 11 mg AgN_3; **d** #91121826, 387 μs, Swine liver confined in a rubber balloon, 10 mg AgN_3, stand-off distance L = 30 mm, 287.2 K; **e** #91121812, 383 μs, Swine liver confined in a rubber balloon, 10 mg AgN_3, L = 50 mm Tw = 301.2 K; **f** #91121815, 368 μs

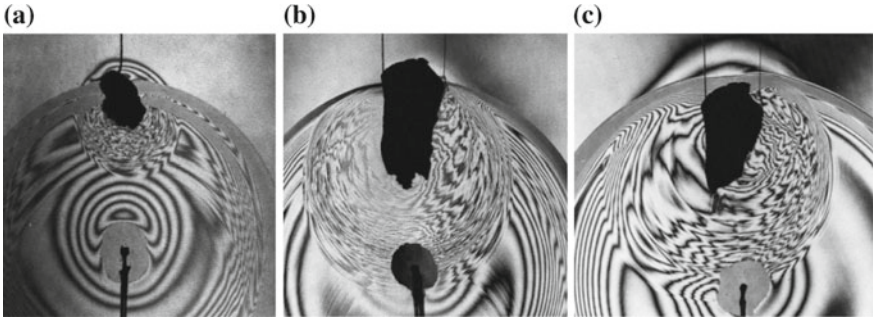

Fig. 10.8 Shock wave interaction with extracted kidney stones: **a** 84051703, dry weight 0.32 g 13 μs from trigger point, 8 mg PbN_6, at 288.7 K; **b** #84052201, 21 μs, 8.3 mg AgN_3, 290.3 K; **c** #84052202, same as #84052201 25 μs, 9.9 mg AgN_3, 290.3 K

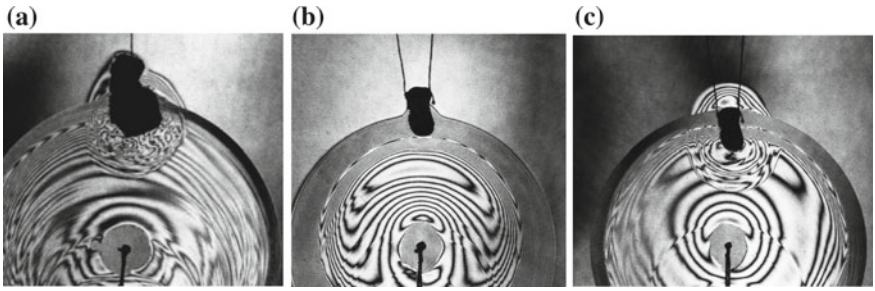

Fig. 10.9 Shock wave interaction with extracted kidney stone; **a** #84051801, dry weight 0.92 g, 12 μs from trigger point, 8 mg AgN_3, 288.4 K; **b** #84052109, 11 μs, 10.2 mg AgN_3, 291.2 K; **c** #84052109, the same as #84052109, 14 μs

10.2.3 In Vitro Experiments

Figure 10.11 shows sequential observation of the disintegration of an extracted kidney stone in vitro taken by 6000 frame/s high speed movie. The shock wave was generated by the explosion of a 10 mg PbN_6 pellet. The kidney stone of 10 mm in diameter and 20 mm in length was placed at the second focal point at 130 mm away from the opening. The inter-frame time was 130 μs. This frame interval was too long to resolve the shock wave. It is, hence, impossible to visualize both a shock wave and kidney stone deformation at the frame rate of 6000 frame/s. Nevertheless, the inception of cavitation bubbles was observed. When the shock wave passed the kidney stone, it instantaneously contracted, although not clearly identified, bulged and then was fragmented. When the stone bulged, the cracks were created on its frontal side.

During clinically experiments, patients did not claim any serious pains. The feeling of pains are totally different depending on gender, age and other factors. Even the identical shock wave over-pressures was loaded, patients claimed pain differently. Some people endured pains caused by over-pressure loading but other people could not. Very little is known about the correlation between feeling of pain and the peak overpressure.

Shock waves created by the explosion of a 10 mg AgN_3 pellet were focused on a kidney stone of the size 10 mm × 20 mm and visualized with a high speed movie with framing rate at 10,000 frame/s. The illumination was a flood light. The sequential images were displayed in Fig. 10.12 (Obara 2001). Unlike direct shadow pictures, the deformation of the kidney stone was still resolved. The shock wave propagated from the left hand side.

In No. 2–7 frames, a few μs after shock wave focusing, cavitation bubbles were generated ahead of the kidney stone. Exposed to the bubble cloud, the stone bulged. In No. 8–15 frames, the bubbles disappeared but still attached on the front side. Upon the exposure of high pressures, cracks were created on the frontal surface. When the bubble detached from the stone, it bulged and then started to contract.

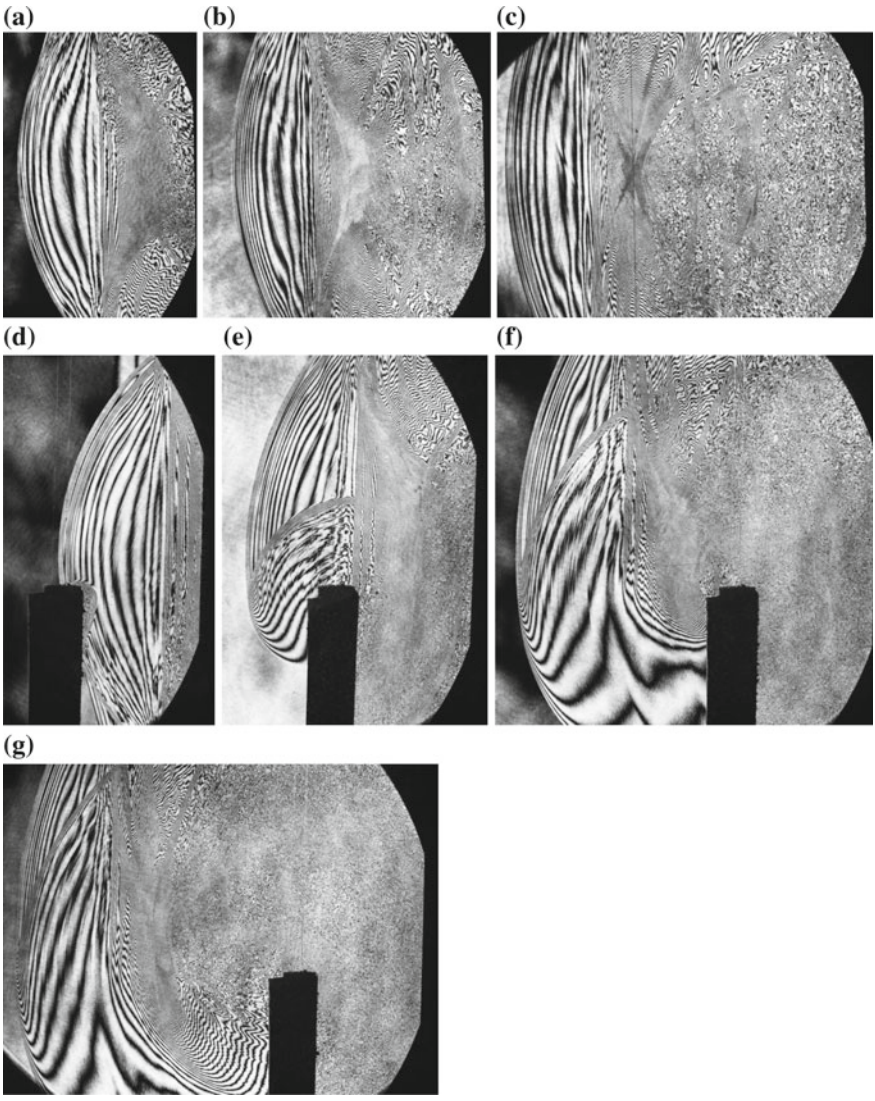

Fig. 10.10 Shock wave focusing from #2 reflector and blockage of focusing by inserting a sponge block at 50 mm from the exit, 10 mg AgN_3 at 288.3 K: **a** #86110108, 80 μs from trigger; **b** #86103003, 130 μs; **c** #86103008, 170 μs; **d** #86110108, 80 μs; **e** #86110106, 100 μs; **f** #86110107, 140 μs; **g** #86110109, 170 μs

The stone was cracked and at the moment when the stone started to expand, the stone started to shatter. The shattering speed is, so far monitored, about 3 m/s, which is too slow to damage tissues.

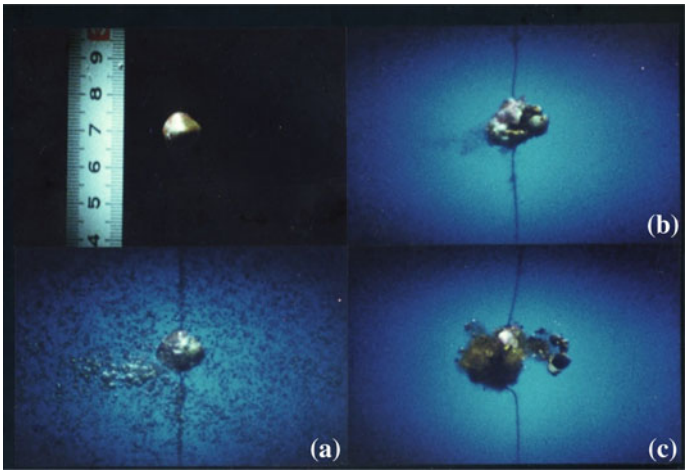

Fig. 10.11 High speed cinematography of disintegration of kidney stone, 6000 frame/s, #83122001

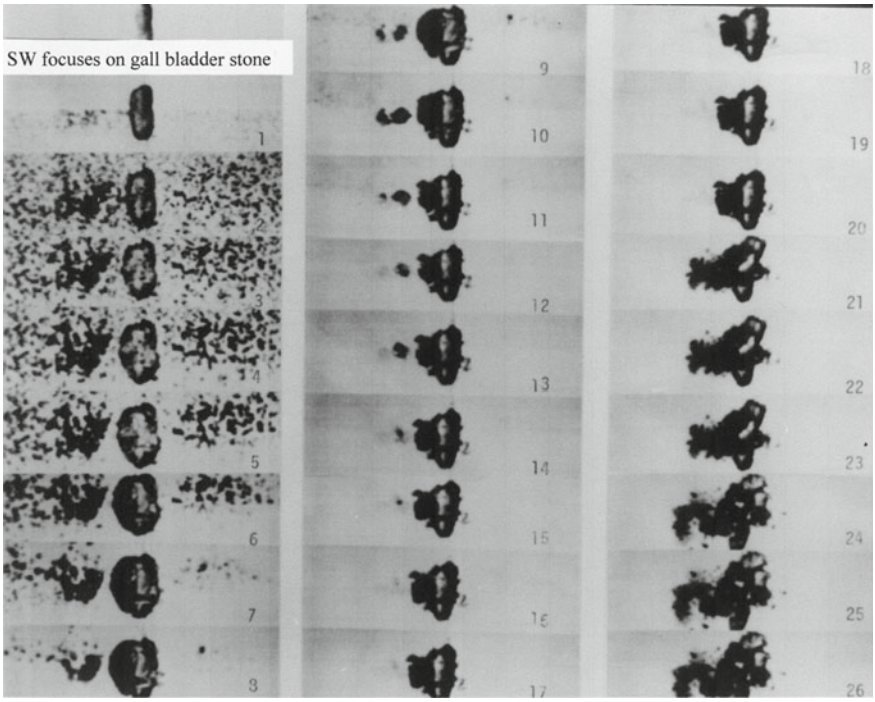

Fig. 10.12 Disintegration of a kidney stone observed at 10,000 frame/s

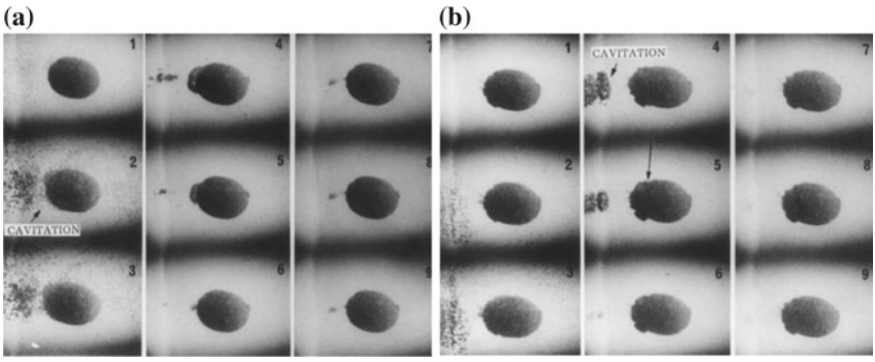

Fig. 10.13 Disintegration of a cholesterol stone 8000 frame/s: **a** first shock exposure; **b** 40th shock wave exposure (Abe et al. 1990)

Figure 10.13a, b show the disintegration of a gallbladder stone. The recording speed was 8000 frame/s and exposure time was approximately 30 μs. An extracted pure cholesterol stone of 20 mm × 25 mm was imbedded in a gelatin layer and placed at the second focal point of a reflector. The gelatin layer was to mimic a gall bladder tissue. Using a reflector having f-number 0.75 and the opening diameter of 180 mm, shock waves generated by exploding a 10 mg AgN_3 pellet and are focused successively 40 times. Figure 10.13a shows the first sequential images.

A pressure was higher than the yield strength of the cholesterol stone. At first the front surface was cracked and then the rear surface. Kidney stones were composed of calcium oxalate, whereas gallbladder stones were composed of cholesterol. Hence the most of gallbladder stones are brittle against a tensile stress, so that their rear surfaces are also cracked by the transmission of reflected tensile stress. After performing shock wave exposures successively for 40 times, the cholesterol stone was fragmented. Figure 10.13b shows a sequence of the 40th shot. In the 5th frame, the stone was momentarily bulged. After the 40th shock wave exposure when opening the gelatin block, the stone was completely fragmented into small sand grains. Once the ESWL was routinely applied to remove gallbladder stones. However, a novel operation by using an endoscope was introduced, the ESWL was no longer used to the removal of the gallbladder stones.

10.2.4 Clinical Experiments

In 1983, Professor Kuwahara decided to commence clinical experiments and applied its permission to the Ethic Committee of the Tohoku University Hospital. The application was granted. Figure 10.14 shows a result of the first clinical experiment (Kuwahara et al. 1986).

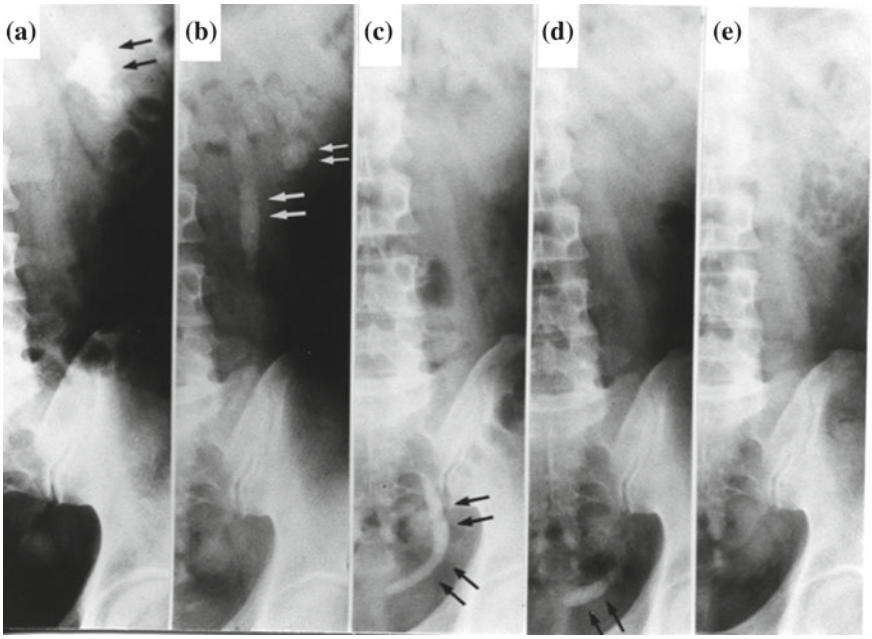

Fig. 10.14 The first clinical application of ESWL using micro-explosions (Kuwahara et al. 1986)

Arrows in Fig. 10.14a indicate a kidney stone before applying the ESWL treatment. After repeatedly focusing shock waves 230 times, the kidney stone was fragmented into sizes of sand grains. Then fragmented kidney stones already discharged out along a ureter. In Fig. 10.14b, fragmented stones formed a street of sand grain. The fragments moved into a bladder in Fig. 10.14c, d. Later, the sand grains were eventually discharged from the body as seen in Fig. 10.14e. Luckily, collaborators with Yachiyoda Kogyo Co. Ltd and Chugoku Kayaku Co Ltd were maintained and eventually a lithotripter using micro-explosives was applied to governmental authorization. In 1987, the Ministry of Health Japan granted the application and the lithotripter was officially used for clinical treatments. This system became one of the unique applications of underwater explosion to the human welfare.

10.2.5 Extracorporeal Shock Wave Induced Bone Formation

Success of ESWL treatments encouraged orthopedic surgeons to apply it to the orthopedic surgery. The treatments of delayed and nonunion of fracture bones are their clinical topics. Ikeda et al. (1999) noticed the ESWL treatment developed in Tohoku University and initiated a collaboration program with us. Dr. Ikeda who is an orthopedic surgeon engaged in the Kanazawa University Hospital, instructed us

the state-in-art of clinical treatments of nonunion fracture bones Ikeda et al. (1999). He expected that if high-pressures generated by shock wave focusing was loaded on nonunion fractured bones, high pressures would stimulate bone formation. To respond to his request, the existing device of ESWL was modified and constructed a device so-named extracorporeal shock wave induced bone formation (ESWLIB).

The ESWL treatment aimed at selectively cracking the urinary tract stones but minimized tissue damages. On the contrary, the ESWLIB damaged tissues creating breeding in the controlled manner in order to unite fracture bones. Then, in the prototype ESWLIB, a strong shock wave is focused by exploding a 30 mg AgN_3 pellet placed at a focal point of a truncated ellipsoidal reflector used for the ESWL. The prototype ESWLIB was applied to animal experiments. Successful animal experiments were expanded to the clinical experiments. The results were successful. Today applications of underwater shock wave focusing to orthopaedic surgery became a routine therapeutic method for not only bone formation therapy but also healing pains in the elbows and the knees.

10.3 Tissue Damages Associated with ESWL

In ESWL treatments, the pressure behind the reflected shock wave increases in propagating toward the focal point. The pressure becomes a maximum when the focusing was completed on a kidney stone surface. In Fig. 10.4, the peak pressure gradually increases toward the focal point and exponentially enhanced in approaching very close to the focal point and became maximal, whereas the entry pressures are so low that the skin surface and the tissue at the entry regions are hardly damaged.

Figure 10.15a is a microscopic observation of damaged cross section of an artery of dog's kidney. In Fig. 10.5d, f, we saw a cavitation bubble cloud and secondary shock waves when bubbles were collapsed. In a bubble cloud, few bubbles survived for nearly one tenth of second (Kuwahara et al. 1989). The life time of bubbles is independent of their source and belongs to matter of probability. Bubbles interact with wavelets or subsequent shock waves and collapse. When collapsing, bubbles eventually create micro-jet. It is a micro-jet that pierces the tissue. A part of the dog's kidney artery looks as if ruptured by a needle in Fig. 10.15. Figure 10.15b shows the traces of shock wave converging into dog's kidney.

10.3.1 Shock Wave Interaction with a Bubble on Gelatin Surface

Tissue damages were caused by either by bubble collapse in the vicinity of the tissue surface or by the high pressure deposition on the tissue. Hence, to reduce the tissue damages, the number of shock wave exposures should be minimized while keeping the efficiency of disintegration of the stones high.

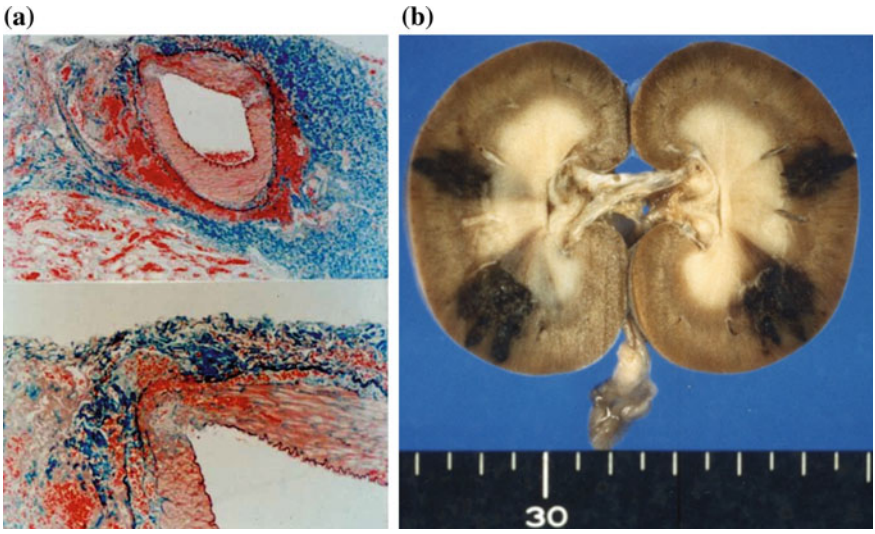

Fig. 10.15 Tissue damage: **a** damage on an artery of dog's kidney; **b** damages on dog's kidney tissues (courtesy of Professor Kuwahara)

To experimentally simulate tissue damage, 8 mm diameter air bubble was placed on a gelatin block and loaded a shock wave by exploding a 10 mg AgN_3 at stand-off distance of L = 30 mm. Figure 10.16 are sequential interferograms. The bubble was contracted forming a jet which penetrated the gelatin. At the same time, the shock wave propagating in the bubble was reflected from the gelatin surface and converged to reverse direction, which formed a multiple jet. It should be noticed that the collapse and jet formation in the bubble is governed by the bubble size and shock wave overpressure. The penetration depth was about 2.5 times as deep as the diameter of bubbles (Shitamori 1990; Obara 2001).

Figure 10.17 show sequential double exposure interferograms of a 1.5 mm diameter air bubble interacting with a shock wave generated by explosion of a 10 mg AgN_3 at L = 50 mm. Unlike Fig. 10.16, multiple reflections of the shock wave in the air bubble were not observable but the jet penetration into gelatin. The tissue damages seen in Fig. 10.15 were created by the collapse of small water vapor bubbles, presumably in the diameter of sub-millimeter. The jet formation presented here were just demonstrating the dynamic of jet penetrations.

Figures 10.17 and 10.18 are double exposure interferograms. A grey shadow was an air bubble placed on a gelatin surface and observed at the first exposure and shadows of deforming bubbles were observed at the second exposure. Upon the shock wave impingement, the bubble started to contract. At the same time the transmitted shock wave was propagating inside the contracting bubble. A jet formed due to the bubble contraction penetrated the gelatin layer. Figure 10.18e shows a remnant of jet penetration. The penetration depth would be affected by the

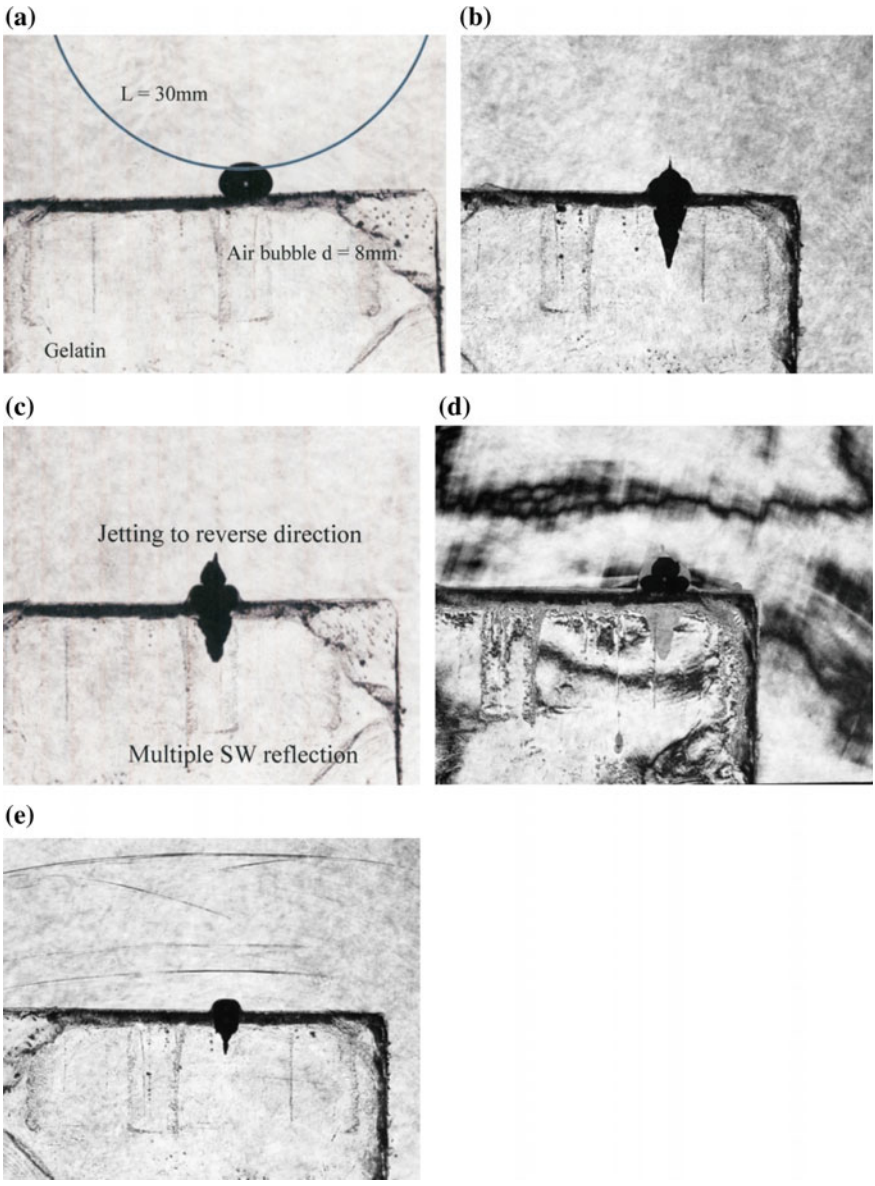

Fig. 10.16 Interaction of a shock wave with 8 mm diameter air bubble on gelatin surface at 296.0 K, 10 mg AgN_3, L = 30 mm: **a** #86090907, 50 μs from trigger point; **b** #86090908, 100 μs; **c** #86090912, 110 μs; **d** #86090913, 130 μs; **e** #86090914, 120 μs

magnitude of stagnation pressures on the gelatin surface. At the moment, no analytical model exists for predicting the stagnation pressure even though assuming a spherical bubble (Shitamori 1990; Obara 2001).

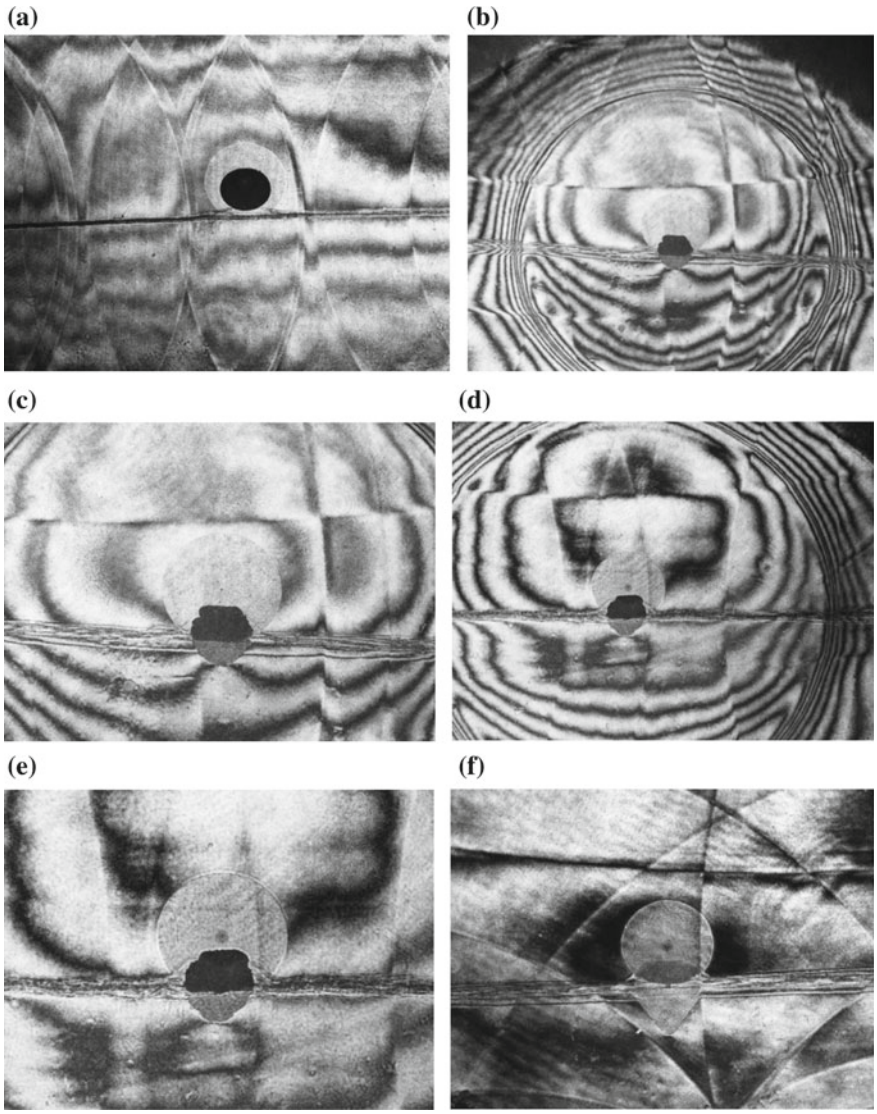

Fig. 10.17 Double exposure interferograms of shock wave interaction with a 1.5 mm diameter air bubble on gelatin surface, a 10 mg AgN_3 at the stand-off distance L = 50 mm at 286.4 K: **a** #85012913, 18 μs; **b** #85012919 23 μs; **c** Enlargement of (**b**); **d** #85012920, 24 μs; **e** Enlargement of (**d**); **f** #85012918, 23 μs

Figure 10.19 show sequential observations of shock wave/bubble interaction recorded by Ima Con High Speed Camera Model 790. Figure 10.19a, b show a 5 mm diameter air bubbles placed on 10 wt% gelatin surface, 5 wt% gelatin surface impinged by a shock wave generated by exploding a 10 mg AgN_3 pellet at the

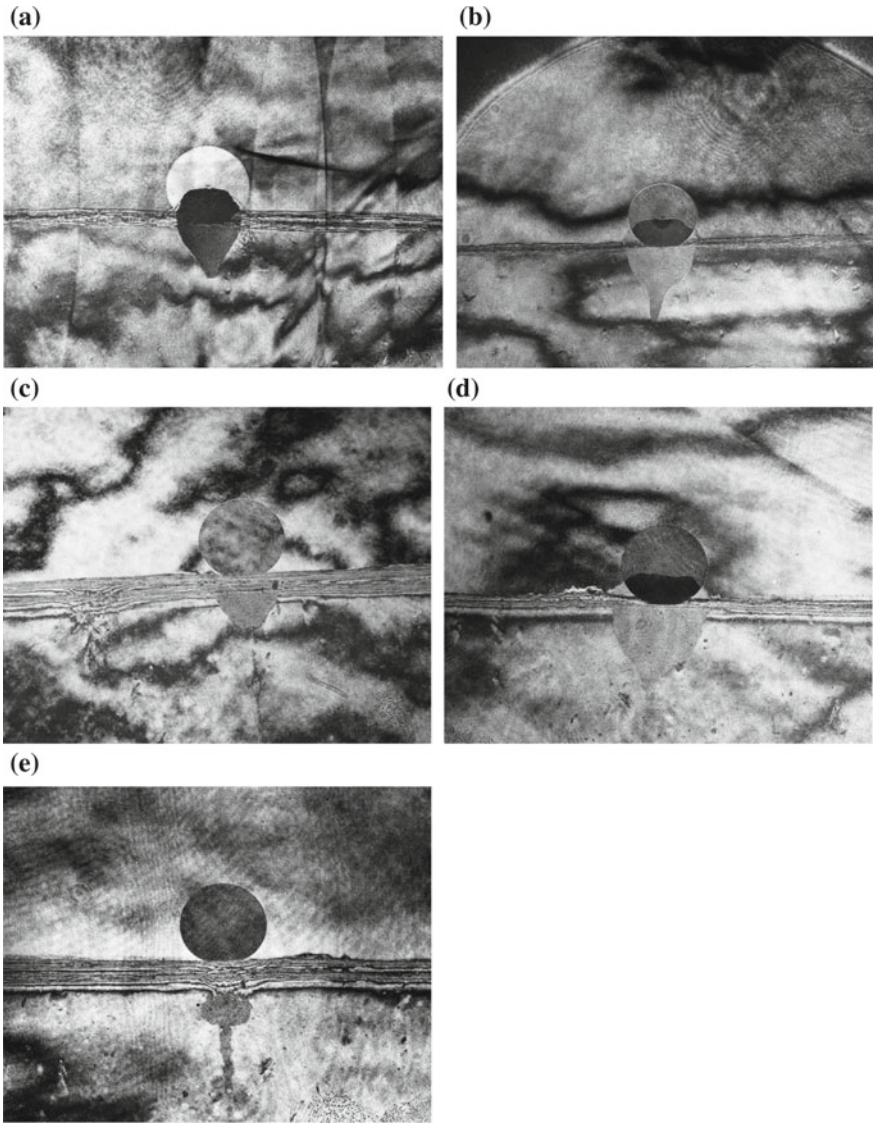

Fig. 10.18 Double exposure interferogram of shock wave interaction with a 3.0 mm diameter air bubble on gelatin surface. Shock wave was generated by exploding a 10 mg AgN_3 pellet at the stand-off distance L = 50 mm at 286.4 K: **a** #85013003 32 μs from trigger point; **b** #85013005 44 μs; **c** #85013105, 125 μs; **d** #85013103 65 μs; **e** #85013104, 95 μs

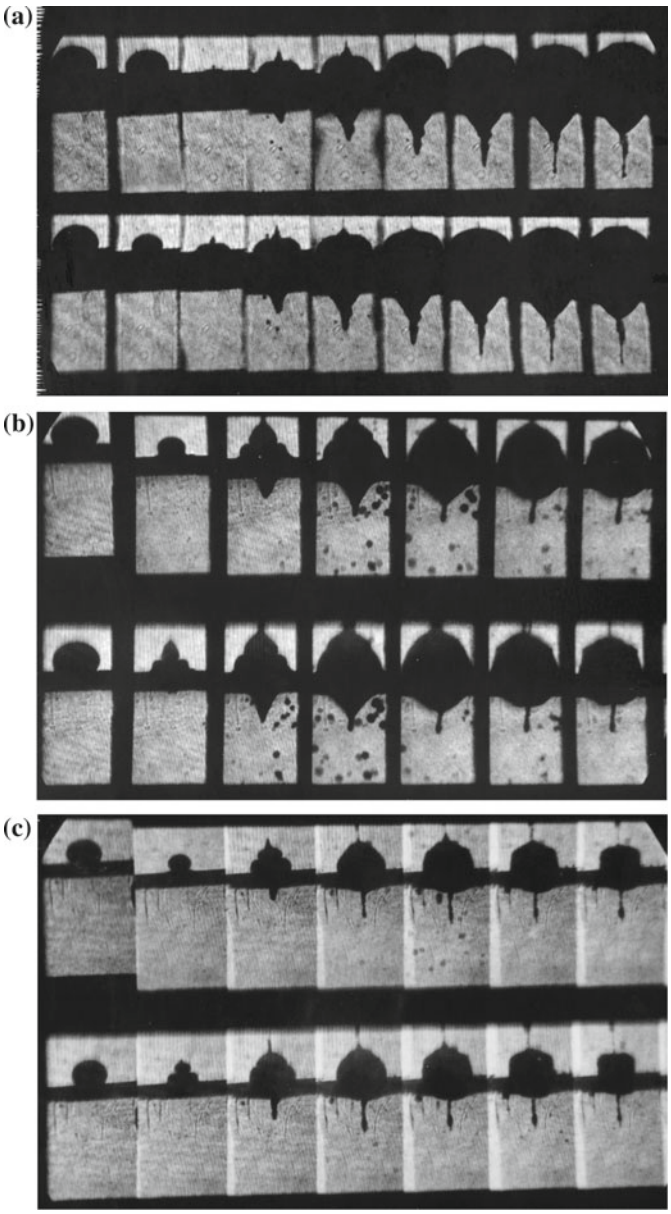

Fig. 10.19 High speed imaging, shock wave interaction with an air bubble placed on a gelatin surface, a 10 mg AgN_3 pellet was exploded at the stand-off distance of L = 50 mm, at atmospheric air, 286.4 K: **a** #90072201, 10 mg AgN_3, 5 mm air bubble at L = 50 mm, on 10 wt% gelatin surface, at 100,000 frame/s, exposure time of 1.25 μs; **b** #91051922, 10 mg AgN_3, 5 mm diameter air bubble at L = 50 mm, on 10 wt% gelatin surface, at 25,000 frame/s, exposure time of 5 μs; **c** #91052014, 3 mg AgN_3, 3 mm diameter air bubble at L = 50 mm, on 5 wt% gelatin surface, at 25,000 frame/s, exposure time of 5 μs

stand-off distance of L = 50 mm. The jet formation toward the reverse direction was observable (Shitamori 1990; Obara 2001). Figure 10.19c shows a 3 mm diameter air bubbles placed on 5 wt% gelatin surface or 10 wt% gelatin surface impinged by a shock wave generated by exploding a 3.0 mg AgN_3 pellet at the stand-off distance of L = 50 mm. The structure of gelatin affected very slightly to the jet penetration.

10.3.2 Domain and Boundary of Tissue Damage in ESWL

Figure 10.20 summarizes the relationship between overpressures and number of the shock exposures. The domain and boundary of tissue damage is shown. The shock waves were generated by focusing of strong sound waves created by a piezo-dish as discussed in Sect. 9.4.5. The ordinate denotes number of shock focusing and the abscissa denotes the over-pressure in MPa. The evaluation parameter of damages is the level of haematoma from a negative bleeding to serious bleeding. Red filled circles denote breeding areas larger than 30 mm^2. Filled orange color circles denote breeding areas from 0 mm^2 to smaller than 30 mm^2. Filled blue color circles denote negative breeding. There are distinct domains and boundaries among damage levels. It is desirable to disintegrate the stones with a minimum level of bleeding by exposing with moderately high peak pressure and at limited number of the shock exposure. Figure 10.20 indicates, however, that the level of haematoma will increase at higher peak pressures and smaller number of shock exposures. At lower peak pressures, the number of shock exposures will increase and at the same time the level of haematoma becomes high. Therefore, the optimum number of shock

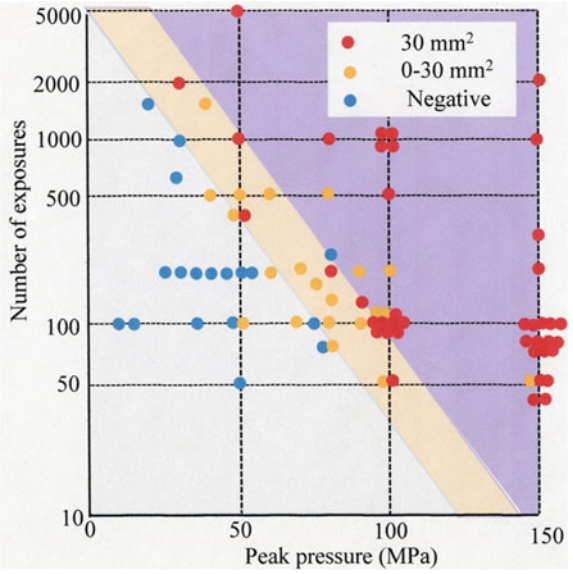

Fig. 10.20 Correlation between number of shock wave exposures and the peak pressures in terms damage level in electromagnetic ultrasound focusing (Okazaki 1989)

exposure will exist which will minimize the level of bleeding. However, the optimized number of shock exposures and the optimized shock strength would depend empirically on the type of stones and their dimension.

10.3.3 Shock Wave Induced Injury on Nerve Cells

Neuro-brain surgeons concerned nerve cell damages caused by shock wave loadings. However, the physical properties of human organs quoted from the literatures which were those collected from extracted tissues differ from those collected from living tissues in the presence of blood circulations (Kato 2004).

Therefore, it was decided to experimentally determine the threshold pressure at which nerve cells are damaged by shock wave loading. A 10 mg AgN_3 pellet was divided into small pieces by using a pair of bamboo tweezers and measured the amount of AgN_3 fragments from 2.5 to 300 μg with a digital precision balance. Figure 10.21 shows a crystal of AgN_3 weighing 2.5 μg. Fragments of AgN_3 were glued, with acetone-cellulose solution, on the edge of 0.6 mm core diameter optical fiber and were ignited by the transmission of a Q-switch Nd:YAG laser beam of total energy of 7 mJ and 20 ns pulse width (Nagayasu 2002).

In order to determine the threshold value of shock wave over-pressure at which nerve cells are damaged, a shock wave was focused on rats' brains accurately at a specified spot using a miniature ellipsoidal reflector. The miniature reflector is a 20 mm × 28.3 mm half truncated ellipsoidal reflector made of brass. Figure 10.22a shows its schematic diagram. Figure 10.22b shows a photograph viewed from its opening.

A shock wave generated by explosion of small AgN_3 pellet was focused at the first focal point of the truncated reflector by transmitting a Q-switched Nd:YAG laser beam through the optical fiber. Figure 10.23a, b show time variation of

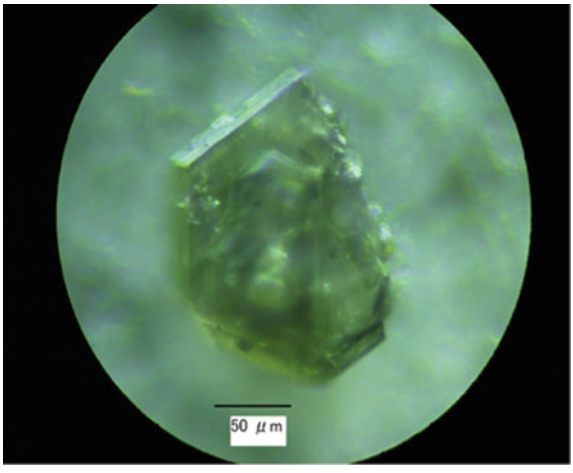

Fig. 10.21 A AgN_3 crystal 2.5 μg in weight

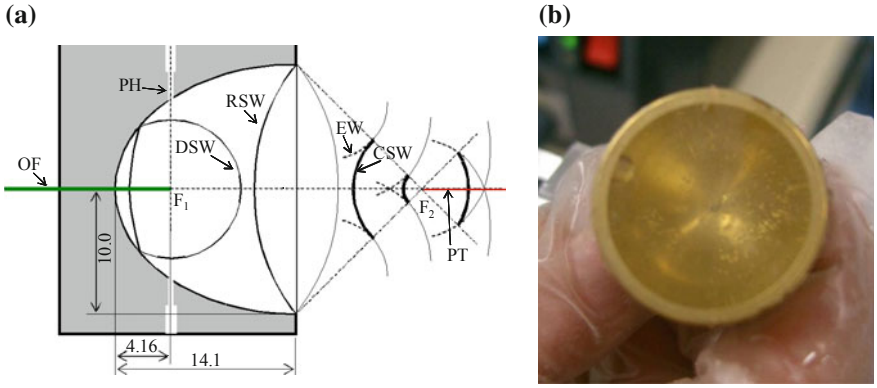

Fig. 10.22 A 20 mm × 28.4 mm truncated ellipsoidal reflector: **a** cross section of the reflector; **b** a view from opening (Kato 2004)

pressures for 2.5 and 15 μg AgN_3 pellets and sequential direct shadowgraphs of the focusing of 2.5 and 15.0 μg AgN_3 pellets. It was noticed that even such small explosives were detonated and their overpressures obeyed the scaling law. The pressures were measured by using optical fiber pressure trasducer.

Eight-week-old male rats were anesthetized and supported on a movable stage. Their right parietal bones were precisely exposed to the focal point. A bone defect of 3–5 mm diameter was made at the right convexity. The bone defect touched a water bath through which the shock wave was focused. A shock wave was generated exploding a 100 μg AgN_3 pellet and focused precisely on a rat's brain. The error of the positioning was less than ±0.1 mm. It was examined the level of overpressure at which the nerve cells were damaged. With this arrangement, high pressures were loaded on rats' nerve cells. The results collected here contributed well to the study of the blast wave injury (Kato 2004). Figure 10.24 shows an experimental arrangement for investigating the threshold pressure of nerve cell injury upon focusing shock wave onto rat's brain.

Figure 10.25 show test results. Shock wave focusing created apoptosis on rat's brain (Kato 2004). Depending on the focused pressure, apoptosis and necrosis occurred. This was an early result of shock/nerve cell interaction. Apoptosis occurs already at a shock wave exposure of 1 MPa.

10.4 Laser Induced Shock Waves for Medical Applications

It is recognized that the ESWL treatment always accompanies tissue damages. There is no exceptional combination of parameters that selectively disintegrates kidney stones without causing any tissue damages. Then it was decided to apply shock wave focusing to damage soft tissues in a controlled manner. Shock waves

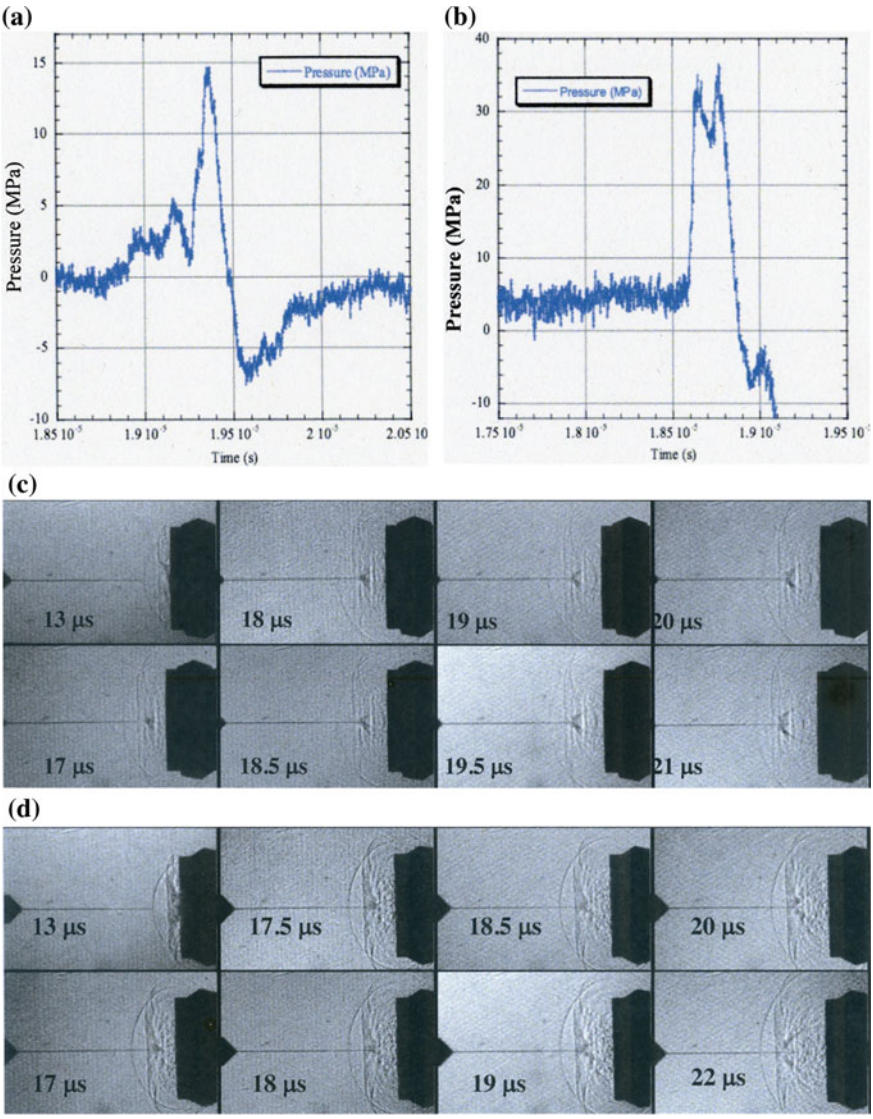

Fig. 10.23 Pressure profile and sequential observation of focusing of shock waves generated by the explosion of 2.5 and 15 μg AgN_3 pellets: **a** pressure profile of 2.5 μg AgN_3; **b** pressure profile of 15 μg AgN_3; **c** shadow pictures of 2.5 μg AgN_3; **d** shadow pictures of 15 μg AgN_3

created by focusing the pulse Ho:YAG laser beams are applied to the revascularization of cerebral thrombosis. This project started under collaboration with the Department of the Neuro-Brain Surgery in the School of Medicine of Tohoku University.

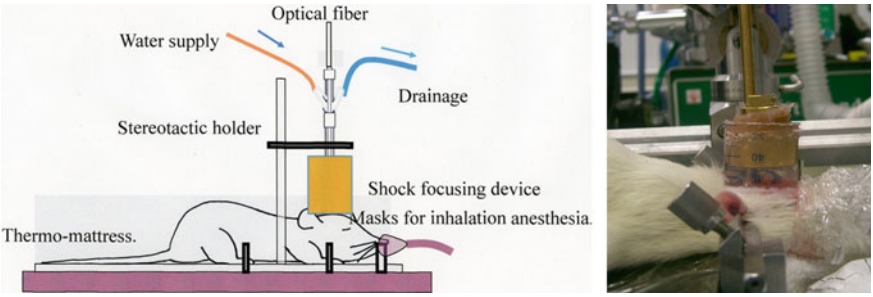

Fig. 10.24 The experimental arrangement of nerve cell injury focusing a shock wave on rat's brain

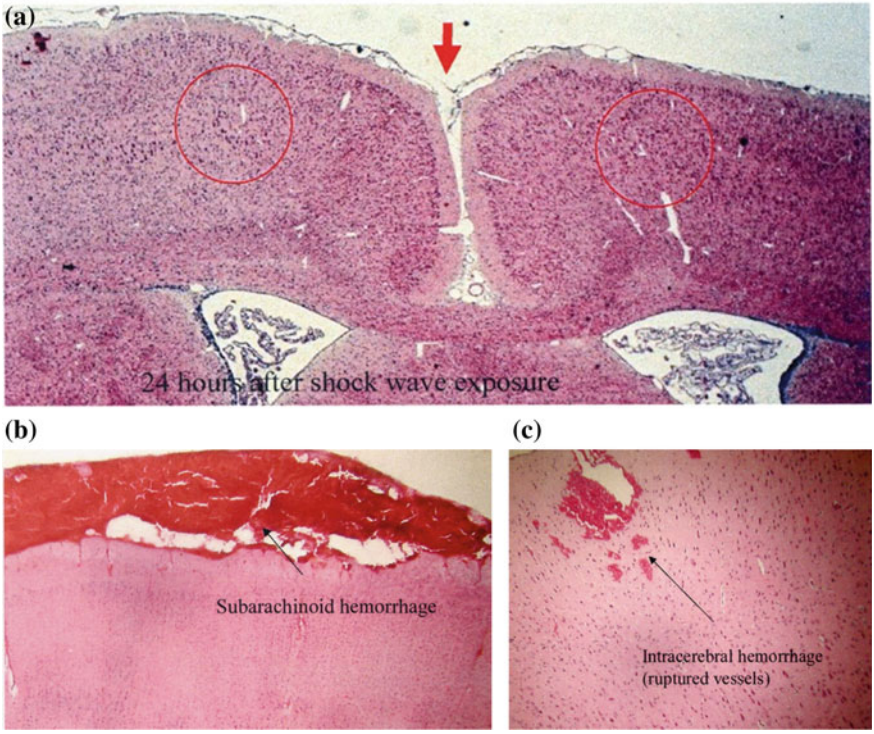

Fig. 10.25 Localized shock wave focusing created apoptosis (Kato 2004): **a** over view; **b**, **c** magnified sections

Laser beams irradiated in water were spontaneously absorbed in water molecules and elevated their energy level to the level of ionization. A water vapor bubble was spontaneously created, which was equivalent to a fire ball of exploding explosives in water spontaneously drove an underwater shock wave.

At first a pulsed Nd:YAG laser of 100 mJ, 130 ns pulse width, and wave length of λ = 1090 nm was focused. Figure 10.26a shows the dependence of absorption coefficient of the laser energy on wave length. The ordinate denotes absorption coefficients of light in water in 1/cm and the abscissa denotes wave lengths, λ in nm. Laser beams having wavelength of visible lights have low absorption coefficients as shown in color spectra which means that the deposition of a Q-switch ruby

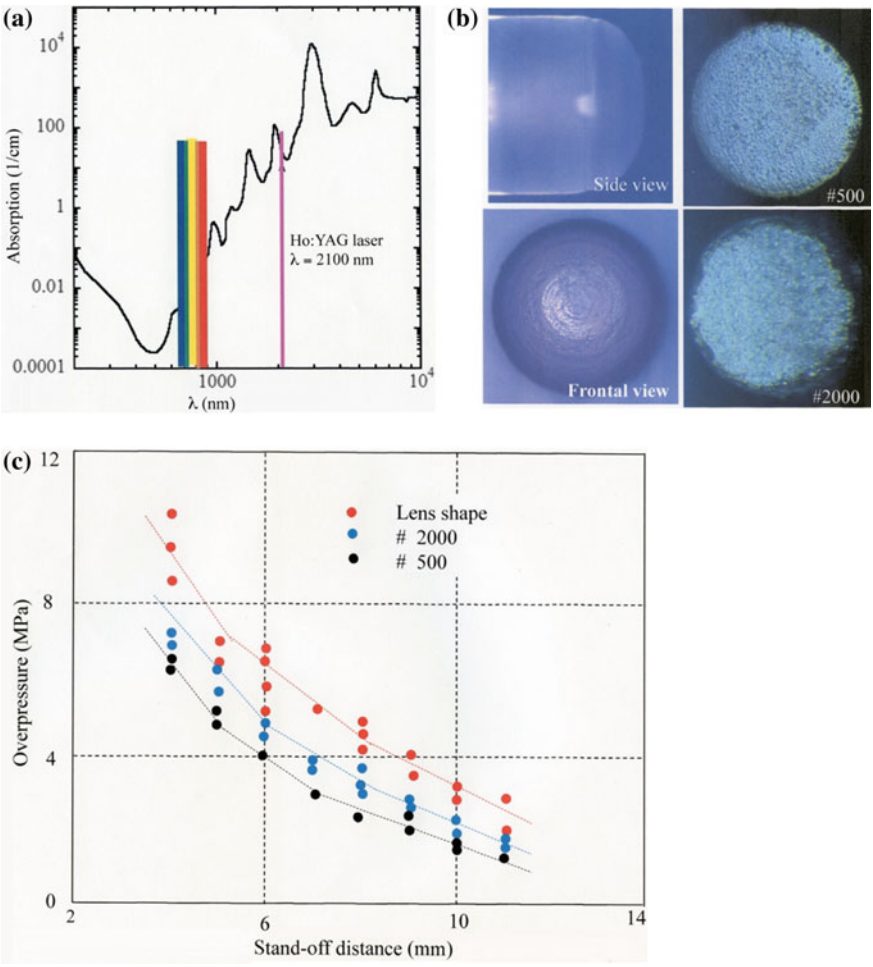

Fig. 10.26 Laser induced shock waves: **a** absorption of laser energy in water; **b** surface finish of ϕ0.6 mm core diameter optical fiber. Edge shape, lens shape, fine and coarse surface finish of #2000, and #500; **c** Shock wave overpressures transmitting 1.0 J Ho: YAG laser beam in MPa versus stand-off distance from the edge in mm

laser having λ = 694.3 nm is less effective for generating shock waves. A Ho:YAG laser having λ = 2100 nm is shown in pink color has the absorption coefficient over 1000 times higher than that of Nd:YAG laser having λ = 1064 nm. The focusing of Ho:YAG laser beam can effectively generate strong underwater shock waves. A Q-switched Ho:YAG laser beam of 1.0 J energy was transmitted through a 0.6 mm diameter quartz optical fiber.

The efficiency of laser beam focusing depends on the surface finish of optical fiber edge. Then the optical fiber edge was polished in a convex lens shape to effectively focus the laser beam and at a point outside the optical fiber.

Figure 10.26b shows shapes of optical fiber edge: lens shape; and flat fine finish edge of a #2000 finish, which indicates the surface roughness equivalence of 2000 grains per inch and a coarse finish #500 which indicates the surface roughness of 500 grains per inch. In Fig. 10.26c, the ordinate denotes the variation of over-pressures in MPa and the abscissa denotes the stand-off distance from the edge of optical fiber in mm. Red, blue and black filled circles denote lens shape, fine and coarse surface finishes of #2000 and #500, respectively. The lens shaped edge generated about 10 MPa over-pressures at the distance about 4 mm from the edge.

Optimal and durable shapes exist but the shapes shown in Fig. 10.26c were deviated far from the optimal one. Lens shaped edges, however, survived in average only for 100 laser transmissions. When inserting an optical fiber into a thin catheter and transmitting the laser beam, shock waves were generated in the vicinity of the edge and the creation of the vapor bubble induced micro water jets impacting the edge surface.

10.4.1 Revascularization of Cerebral Thrombosis

In order to visualize the generation of the bubble and formation of shock waves in a catheter, visualization was conducted using a 5 mm diameter and 60 mm long aspheric lens shaped cylinder made of acryl. Figure 10.27a shows an aspheric lens shaped thin tube. Figure 10.27b shows irradiations of a Q-switched laser beam having 91 mJ/pulse and 200 ns pulse width inside the aspheric lens shaped test section. A solid line along the axis show a lens shaped optical fiber. In Fig. 10.27b, the first 6 frames show sequential observation at the time interval of 1 μs. The arrows indicate the shock waves. In the second 6 frames, the first image was taken at 2 μs and the other frames started from 350 μs at the time interval of 50 μs, the increase in the bubble diameter was clearly observed. The shock wave propagation and flows in a 5 mm diameter tube are clearly observed (Ohki 1999).

Q-switched Ho:YAG laser beams repeatedly transmittomg through a 0.6 mm optical fiber can created shock waves at its edge. The shock wave can just penetrate the surface of artificial thrombus filled in a thin tube. Figure 10.28 show sequential penetration of the thrombus with successive shock wave impingements. Indeed it worked but not very efficiently. The optical fiber had a lens shaped edge so that the

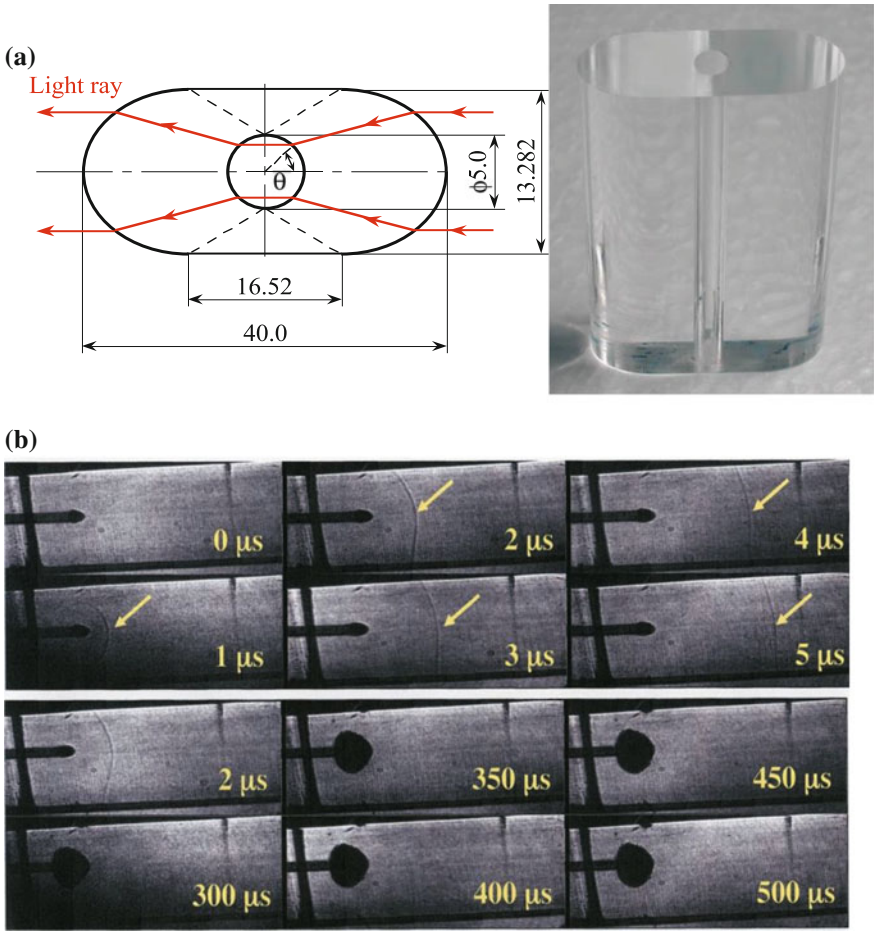

Fig. 10.27 Laser induced shock waves in a 5 mm diameter aspheric lens shaped tube, Q-switched Ho:YAG laser beams having 91 mJ/pulse and 200 ns pulse duration were transmitted through a 0.6 mm core diameter optical fiber: **a** aspheric lens shaped 5 mm diameter tube; **b** formation of a shock wave 0–5 μs, formation of bubble from 2 to 500 μs

resulting shock wave over-pressures were high enough to readily penetrate the thrombus. Figure 10.28 shows the optical fiber edge penetrating the artificial thrombus by successive irradiation of Q-switched Ho:YAG laser beams. The idea indeed worked but the penetration proceeded too slow. Encouraged by the result seen in Fig. 10.28, an extension tube was attached at the edge of the catheter. The extension tube transmitted a water jet to a position away from the edge of the optical fiber.

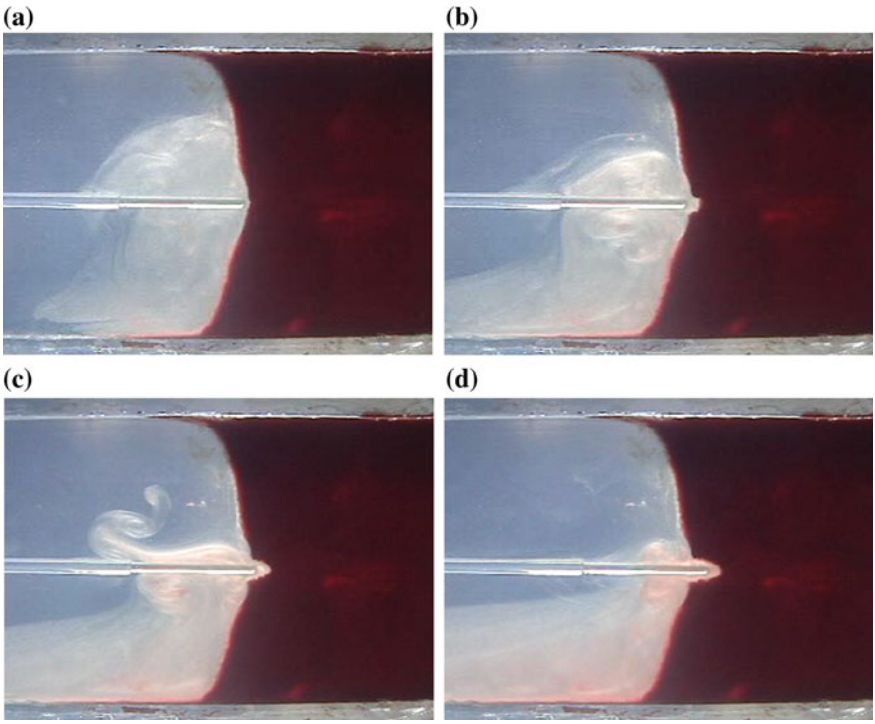

Fig. 10.28 Penetration of an artificial thrombus by Ho:YAG laser beam irradiation (Hirano et al. 2002)

10.4.2 Catheter of Dissecting Soft Tissue

10.4.2.1 Laser Induced Dissector

After conducting in vitro tests, a relatively long extension tube was connected to the open end of a catheter so as to reach the middle cerebral artery. Figure 10.29 shows the prototype catheter.

Pulsed Ho:YAG laser beams having pulse width of 350 ns and frequency of 3 Hz, and maximum energy of 1.3 W were transmitted through a 0.6 mm core diameter optical fiber. The optical fiber was inserted in a 4 Fr and 20 mm long stainless steel catheter and a 2.7 Fr and about 300 mm long flexible tube was connected at the edge of the catheter. Then water jets were ejected at the volume rate of about 13 mm^3/s at each laser irradiation. This volume rate was little readily to aspirate. Then to assure its effectiveness, an in vivo experiment was conducted: a swine artery was choked with thrombi and a prototype catheter was applied to penetrate the thrombi.

Figure 10.30 shows the sequence of X-ray monitors. Yellow circles show the artery under study. At first the artery was choked with thrombi and the blockage of

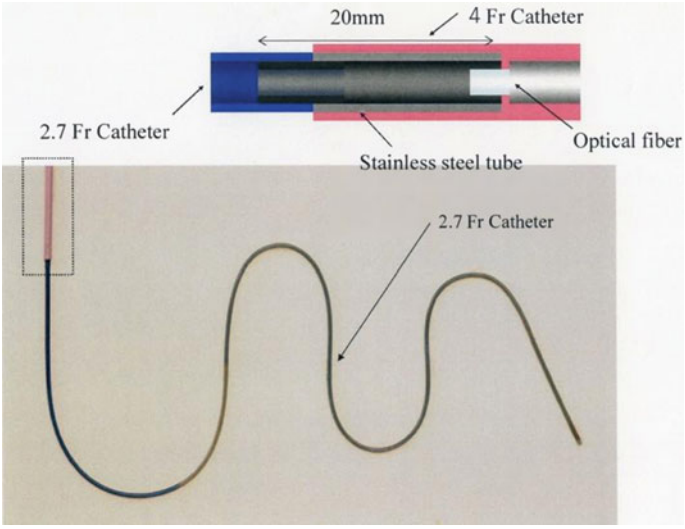

Fig. 10.29 Ho:YAG laser induced dissection catheter

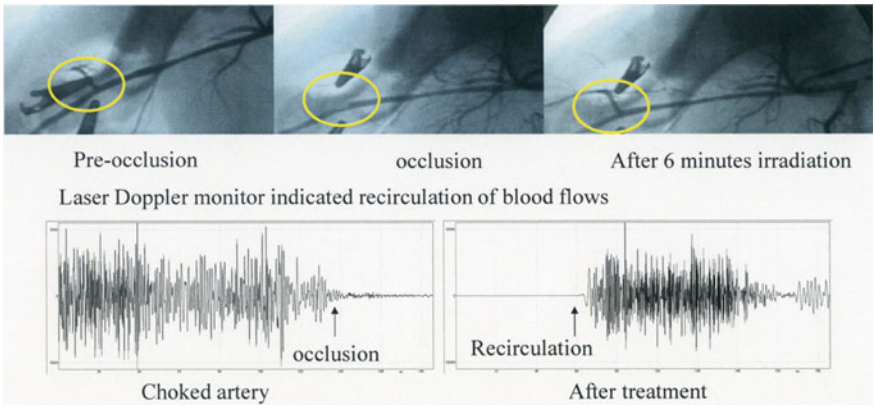

Fig. 10.30 In vivo experiment of revascularization of thrombosis of a swine artery

the blood circulation was confirmed. After applying laser irradiation for 6 min at 3 Hz, the blood circulation restarted. It was convinced that the catheter succeeded the revascularization of thrombosis. The prototype catheter consumed extremely small amount of water only a few cc of water for one sequence.

Throughout in vivo experiments, the final goal of revascularization of cerebral thrombosis was found to be a benign subject to achieve (Hirano et al. 2002). Hence, the goal of the project was shifted to develop a device for dissecting soft tissues: the removal of brain tumors. Figure 10.31a shows an illustration of a prototype catheter

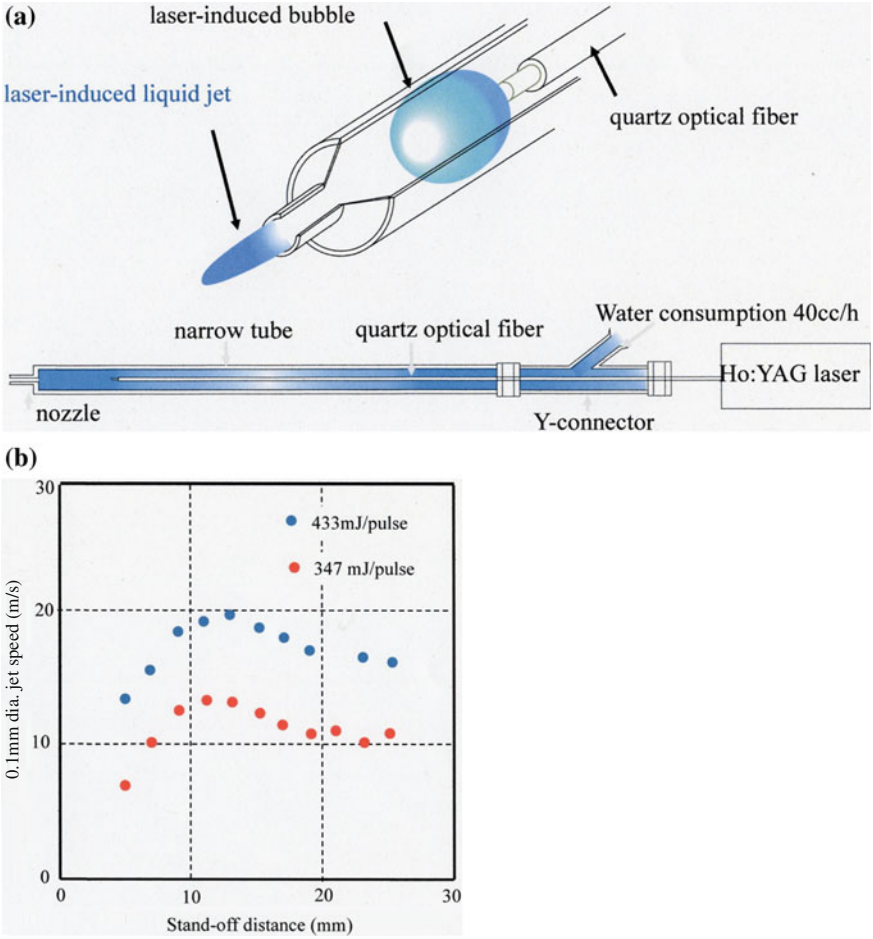

Fig. 10.31 A prototype of dissection catheter: **a** schematic structure of a catheter; **b** jet velocity versus stand-off distance (Hirano et al. 2002)

equipped with a 0.1 mm diameter nozzle. A pulsed Ho:YAG laser of wave length of 2100 nm, pulse width of 350 ns, and 3 Hz was transmitted through a 0.6 mm quartz optical fiber and inserted into a narrow tube from its end. Water was ejected from a 0.1 mm diameter nozzle intermittently at volume rate of 13 mm^3/s at every laser irradiation. Water was continuously supplied from the end of a Y-connector. Hence, the jet speed varies depending on the amount of the laser energy. Figure 10.31b shows the relationship between the jet speed and the laser energy. The ordinate denotes jet speed in m/s and the abscissa denotes the distance from the nozzle exit. Blue and red filled circles denote the laser energy of 433 and 347 mJ/pulse, respectively. The jet speed increases with increasing laser energy. However, the jet speed is maximal at the stand-off distance of about 18 mm.

Figure 10.32a show a sequential observation of a 0.1 mm diameter jet penetrating into a gelatin block visualized every 256 μs interval. The laser energy was 433 mJ/pulse at frequency of 3 Hz. The penetration speed was about 0.5 mm/shot. It is observed that the jet slowly penetrates the gelatin block. Figure 10.32b shows a result of in vivo experiments. A piece of extracted pig liver was dissected using a prototype dissection catheter. The specimen was successfully dissected but the thin blood vessels were preserved. It is concluded that 0.1 mm diameter jets are able to successfully dissect soft tissues and to preserve over 0.2 mm diameter blood vessels. In clinical tests of removing brain tumors, the brain tumor was removed with slightest bleeding as blood vessels of diameter over 0.2 mm were preserved. The catheter had an aspiration tube. The catheter weighed less than 100 g so that it was easy to hold in hand (Nakagawa 1998).

Figure 10.33a shows a clinical application of the dissection catheter to the removal a temporal insular glioblastoma (brain tumor). As the catheter had an aspiration, jet water and the remnant of bleeding were not observed in the field of view. The jets preserved blood vessels of diameter less than 0.2 mm so that the field of view was not disturbed by bleeding not a flood of jet water. The water jet speed can reach about 10–15 m/s and hence its stagnation pressures are high to readily rupture or pierce thin blood vessels. However, it will occur, if 0.1 mm diameter water jet may impinge sharply perpendicularly on the surface of blood vessels exceeding 0.2 mm diameter. During the surgical operation, the catheter was held by hand so that the water jet would impinge obliquely on thin blood vessels. Therefore, blood vessels over 0.2 mm diameter are preserved.

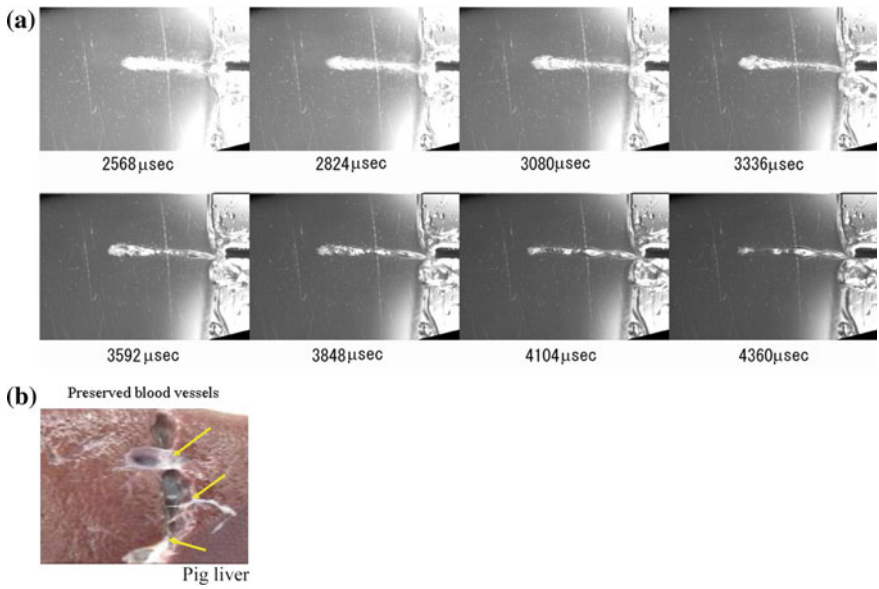

Fig. 10.32 Examples of dissecting catheter: **a** penetration into a gelatin block; **b** dissection of pig liver

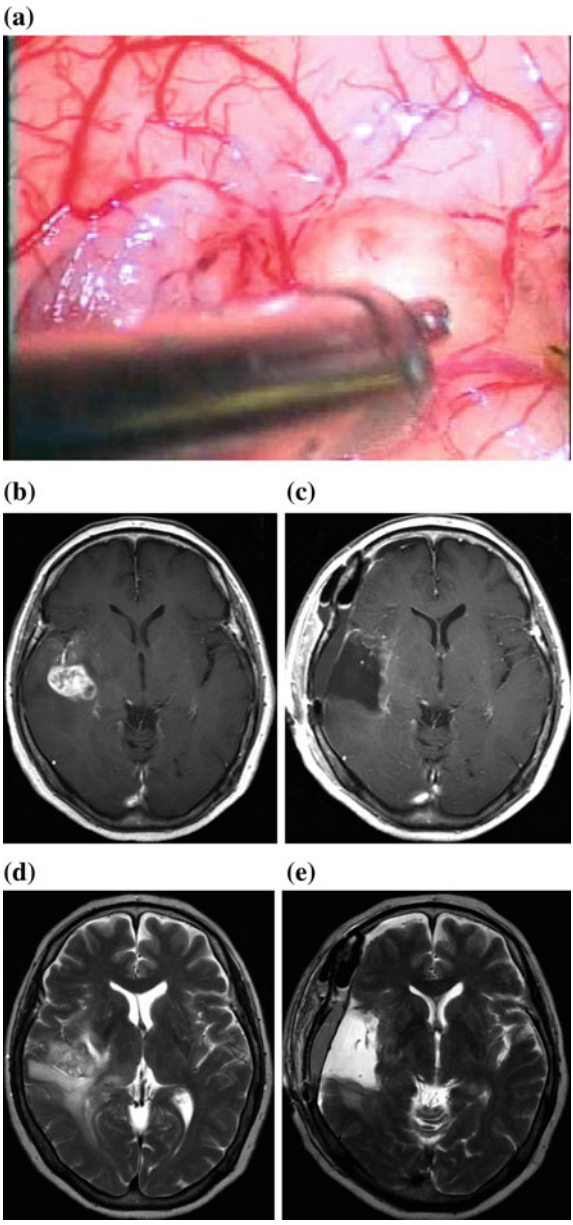

Fig. 10.33 The results of clinical treatment of a jet dissection catheter applied to temporal insular glioblastoma: **a** application to clinical test; **b** X-ray image before treatment; **c** X-ray image after treatment; **d** CT image, before treatment; **e** CT image, after treatment (Nakagawa et al. 2008)

Figure 10.33b, c show X ray images before and after the operation. Figure 10.33d, e show CT images before and after the operation. The tumor was removed but neighboring vessels were not damaged. The results were successful and hence it is expected to have the approval of the Ministry of Health, Japan (Nakagawa 2008).

10.4.2.2 Piezo Actuator

The amount of water ejected at a single movement of the actuator moving robot arms was at most a 0.1 mm^3. This volume water is equivalence of the amount of water required to dissect soft tissues needed for laser induced soft tissue dissectors. Then a robot arm technique was converted to intermittently drive micro water jets applied to the dissection of soft tissue. Figure 10.34a, b show an actuator driven jet generator and its structure. The actuators are inexpensive and commercially available so that a prototype catheter can be compact and has a light weight.

Figure 10.35 shows streak photographs of actuator driven jets at 800 Hz. The jets were generated using nozzles diameter 0.1, 0.15, and 0.2 mm. The ordinate denotes the distance from the jet opening in mm and the abscissa denotes elapsed time in ms. Hence, the inclination angles of the streak images indicate the jet speed. In the case of 0.15 mm nozzle diameter, the jet is ejected in a regulated manner, and

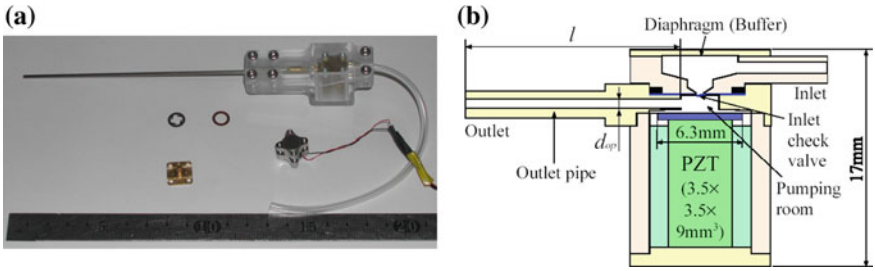

Fig. 10.34 Soft tissue dissection device: **a** prototype device; **b** Illustration of structure

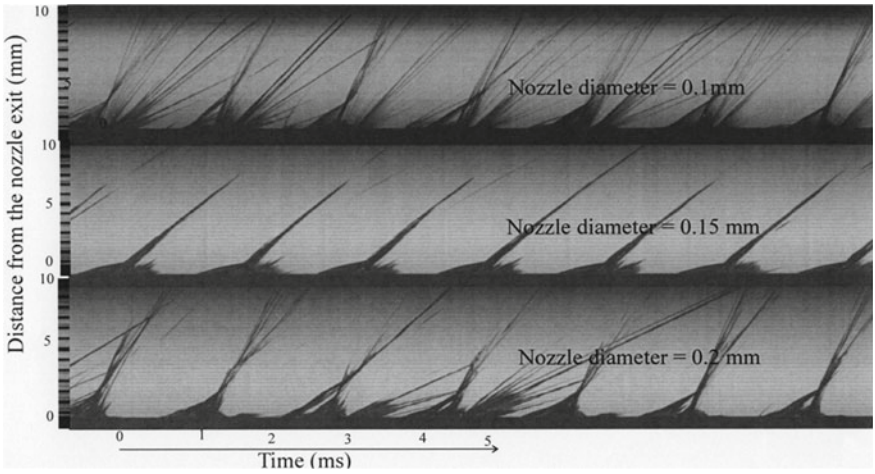

Fig. 10.35 Streak recording of jet formation at variable nozzle diameters

its ejection speed is about 45 m/s, whereas in the case of 0.10 and 0.2 mm diameter nozzles, the shadow of the jet fluctuate randomly which corresponds to the fluctuation of the jet speeds. Hence the nozzle diameter 0.15 mm was found to achieve the optimum combination of the parameters.

10.4.3 Laser Assisted Drug Delivery

Application of a compact gun to a drug delivery method was reported, for the first time, in Nature (1987), in which minute drug particles attached on a metal plate were ejected at high speed, The metal plate is impinged by a high-speed projectile from behind. Particles moving at high-speed penetrated into tissues and created a drug delivery effect. Therefore, this system was named as a particle gun. Figure 10.36 shows mechanical drug delivery methods reported in open literatures. These methods are more or less related to high-speed flows or applications of shock waves.

Gold particles of 1 μs in diameter coated with DNA were driven by high speed flows and impacted into plant seeds. This method proposed by DuPont initiated the recombination of DNA in plant cells and today intensively used in agriculture. The high speed flow was created by rupturing a diaphragm which sealed high pressure helium and working air. The principle is exactly the same as a shock tube.

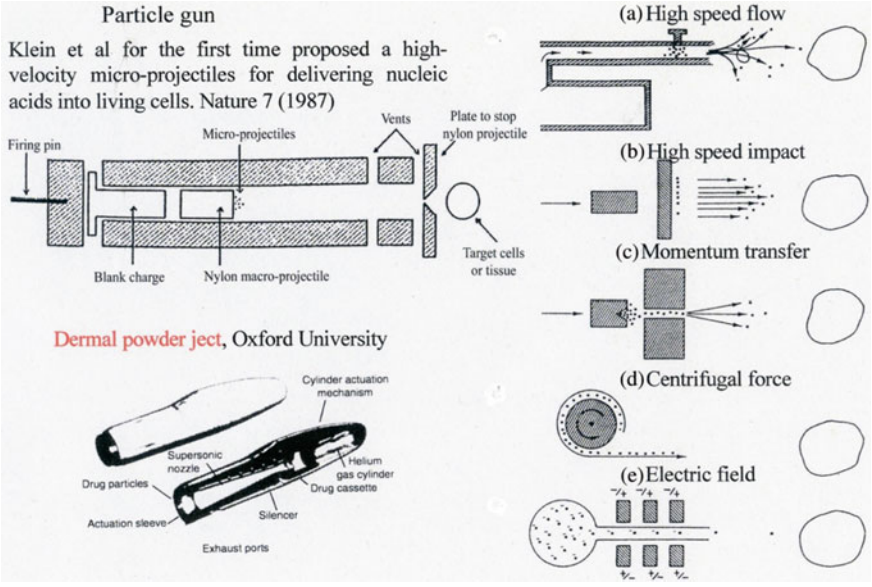

Fig. 10.36 The methods of previous drug delivery

The dermal powderject was invented by Professor Bellhouse et al. (1997) of Oxford University and was already used in clinical treatments. Various drug delivery methods are proposed as shown in Fig. 10.36. As reported in this Chapter, a laser induced drug delivery system is presented.

Figure 10.37 shows, as an analogue experiment of a laser induced drug delivery, shattering of polyethylene beads of 4.8 mm diameter attached vertically in a line on a steel plate. The steel plate was impacted with a nylon piston from behind. The steel plate's sudden deformation ejected the beads. The images were recorded by direct shadowgraph at the framing rate of 10^6 frame/s by Shimazu digital video camera SH100. In Fig. 10.37a, when a 50 mm diameter and 50 mm long nylon cylinder impacted the target steel plate at 340 m/s, an impact flash was emitted at the reverse side. The beads vertically arrayed were just about to be projected. The nylon cylinder squeezed into the target and quickly bulged the thin steel plate. Then the beads were ejected in air. Bow shock waves were formed in front of the beads as seen in Fig. 10.37c–f.

Figure 10.38 schematically explain the laser induced drug delivery system and shows a 100–150 μm thick aluminum foil on which 1 μm diameter gold particles were attached and overlaid a 10 μm thick BK7 glass plate. When a Q-switched high power laser beam having a 2 mm diameter flat head shape irradiated the aluminum foil through the overlaid glass plate, the aluminum plate absorbed the laser energy and a plasma cloud was instantaneously generated on its surface between the foil and the BK7 glass plate. The laser energy deposition was very similar to the explosion of a 2 mm diameter explosive on the surface of the aluminum plate and then the equivalence of the explosion product gas was the aluminum plasma confined between the glass plate and aluminum foil. The plasma cloud explosively

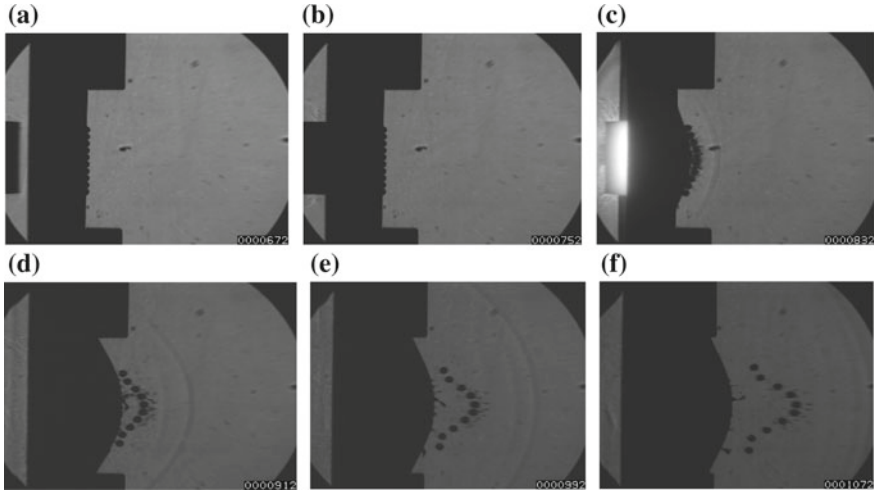

Fig. 10.37 Propulsion of 4.8 mm polyethylene beads attached ln a line on a steel plate hit by a nylon cylinder at 340 m/s

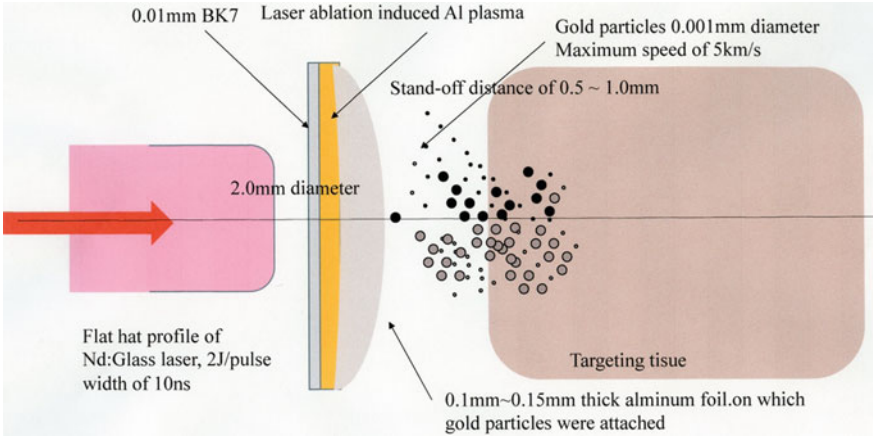

Fig. 10.38 Schematic illustration of pulse laser induced drug delivery

bulged the Al foil and ejected 1 μm diameter gold particles attached on the surface at maximum speed of 5 km/s (Menezes et al. 2008). The gold particles were ejected to targeting tissues positioned at about 1–1.5 mm stand-off distance and penetrated into the targeting tissue. The penetration depth ranged from 0.1 to 0.15 mm stand-off distance.

When dry drug particles are attached on the surface of the aluminum foil as a replacement of gold particles, the abovementioned method becomes a laser ablation assisted particle drug delivery system. The dry drug articles would fly at hypersonic speed when ejected from the foil and soon attenuated to a low supersonic speed. The particles would then penetrate targeting tissues deeply. Just from gas dynamic curiosity, a flow having Ms = 10 and the Reynolds number Re = 100, and Knutsen number Kn = 0.1 is defined as a Hypersonic Stokes flow. However, the distance the dry particles fly would range from 0.5 to 1.5 mm. Although the flow under study is a Hypersonic Stokes flow, effects of aerodynamic heating would not affect the penetration of dry drug delivery aa the rate of heat transfer is too slow.

Figure 10.39a shows an experimental result of shattering of 1 μm tungsten particles in air. The ordinate denotes the speed of particle clouds in m/s and abscissa denotes the flight distance in mm. The open circles denote results measured from the high-speed images. The particles were ejected using a similar system as shown in Fig. 10.38. The motion of the cloud of tungsten particles visualized by direct shadowgraph and images were recorded by high speed video camera Shimadzu SH100.

The particles moved at hypersonic speeds for a few mm distance and soon attenuated. Figure 10.39b shows the penetration of 1 μm diameter tungsten particles into a pig liver placed at 1 mm stand-off distance from the foil on which tungsten particles were attached. The particles were shattered but the central part of the distributed particle penetrated deeply into the pig liver. The particles penetrated

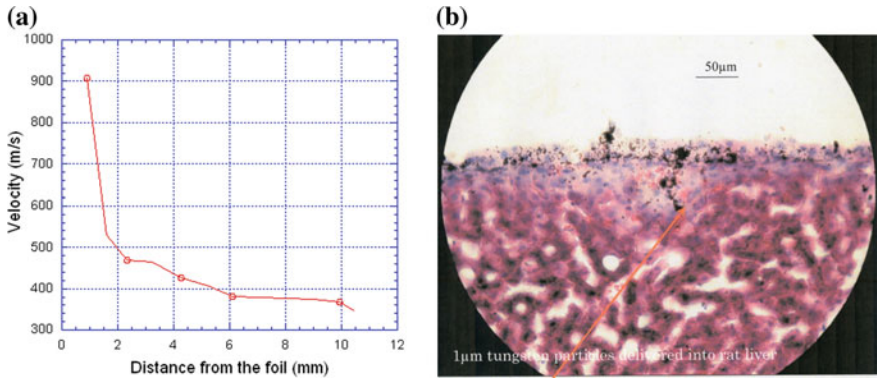

Fig. 10.39 Injection of 1 μm diameter tungsten particles: **a** the particle cloud velocity m/s versus the stand-off distance; **b** penetration test (Menezes et al. 2008)

about 100 μm deep. When this system is applied to the DNA recombination, the use of metal particles is not desirable. It would be a wonderful improvement in the drug delivery methods, if liquid droplets of diameter ranging from 10 to 20 μm can be shattered at reasonably high speed and can penetrate into soft tissue at 50 μm in depth.

Figure 10.40a shows a microscopic observation. It is clearly observed that a 1 μm diameter tungsten particle penetrated a cell line. If the tungsten particle was coated with DNA, there will be chances to have the DNA recombines. In using a shock wave induced drug delivery system, it became a routine methodology to recombine plant cell DNA by means of dry drug delivery system. Figure 10.40b shows the injection of 1 μm gold particles coated with a plasmid DNA into onion cells. In Fig. 10.40c, a gene expression in onion cells was observed. The colored spots indicate the transformed cells in the onion cells. The observation indicates that the present laser ablation induced drug delivery method worked (Nakada et al. 2008).

10.4.4 Shock Wave Ablation Catheter

To cure arrhythmia, the high radio frequency ablation catheter, the so-called ablation catheter is used clinically. In this treatment, high radio frequency eradicated an arrhythmia source in the heart and then the nerve cell at the arrhythmia source was completely destroyed and then the symptom disappeared. However, the radio frequency ablation induced high temperature on the spot at which the ablations were repeatedly applied subsequently inducing thrombi. This would create embolisms in a high probability.

In order to overcome such side effects and eradicate arrhythmia, a shock wave ablation catheter was proposed. In this proposed method, high pressures were

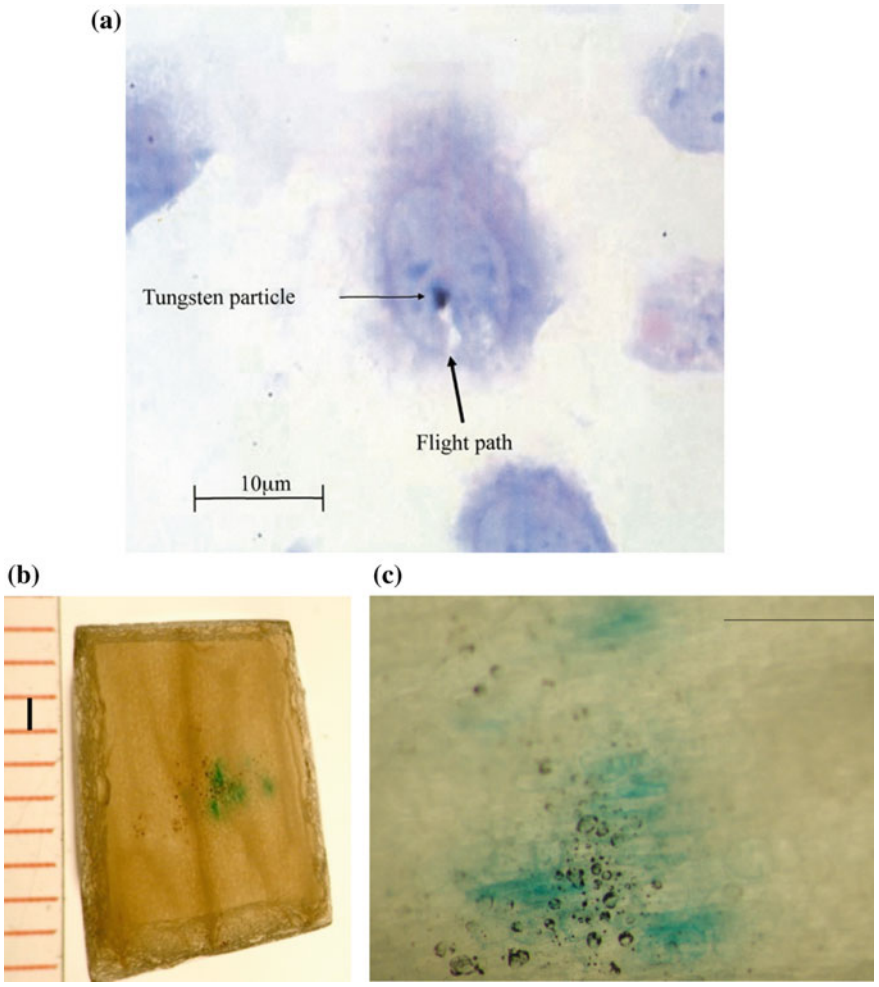

Fig. 10.40 Laser ablation induced drug delivery: **a** 1 μm diameter tungsten particles injected into cell line; **b** gene expression appeared in onion cells; **c** enlargement of (**b**) (Nakada et al. 2008)

applied very locally to the arrhythmia source by the shock wave focusing already applied to ESWL treatments. However, the proposed catheter was inserted into patients' artery to the inside heart so that the diameter of the truncated ellipsoidal reflector was less than 4 mm opening diameter and the source of shock wave generation was a Q-switched Ho:YAG laser beam transmitted via 0.4 mm diameter optical fiber (Yamamoto et al. 2015). Figure 10.41 shows a truncated ablation catheter which is going to be inserted through an artery to a spot inside the heart at which the arrhythmia source is located. The truncate ellipsoidal cavity had its inner diameter of 4.0 mm and outer diameter of 5.6 mm, whose *f*-number was about 0.5.

Fig. 10.41 Prototype of a shock wave ablation catheter (Yamamoto et al. 2015)

Empirically the energy transmission of the reflector in this *f*-number is maximal. The laser beams were transmitted repeatedly in such a confined space for 100 times during one sequence and then the water temperature in the space was elevated. Then saline water is continuously circulated. However, the degree of the elevated temperature was negligibly low.

Then, the catheter is covered with a thin film which is not only disconnecting the cooling saline water circulating inside the reflector but also its leakage into the blood inside the heart. While treatments, the cavity touched the internal membrane of the heart but the pressure at the exit of the cavity was low so that the internal membrane was not damaged. During the shock wave focusing, the peak pressure was gradually increased and exponentially enhanced in the vicinity of the focal point so that the arrhythmia source area was selectively damaged.

Pulsed Q-switched Ho:YAG laser beams of 35 mJ/pulse were repeatedly transmitted at 3 Hz through a 0.4 mm diameter optical fiber. Laser beams were focused through a lens shaped edge and created repeatedly shock waves. Figure 10.42a shows a sequential observation of a shock wave focusing. The ellipsoidal cavity was positioned at the bottom. The shock wave was going to focus at about 2 mm away from the opening of the truncated ellipsoidal cavity and focusing pressure was measures by an optical pressure transducer placed at the upper part in Fig. 10.42a. Figure 10.42b shows the resulting focused pressure. The ordinate denotes pressure in MPa. The abscissa denotes time in μs. The origin was the time instant when the pressure was maximal. Peak focus pressure was about 50 MPa and its half width is about 100 ns, which is strong enough to damage the arrhythmia source. As seen in Fig. 10.42a, the pressure gradually increases toward the arrhythmia source and exponentially enhanced at about 2 mm depth. Hence the tissue at the surface is not damaged seriously.

Figure 10.43 shows the result of a shock wave focusing on rat's heart from three different directions. For each direction, shock waves were focused at peak pressures

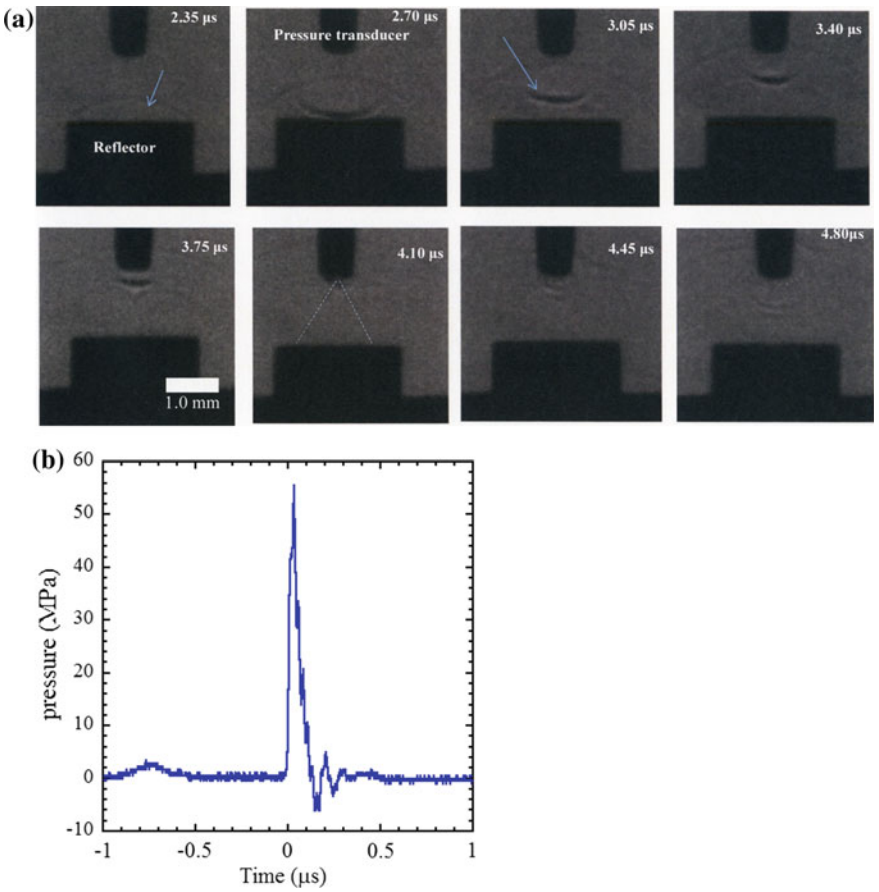

Fig. 10.42 Ho:YAG laser focusing: **a** focusing of a Q-switched Ho:YAG laser; **b** pressure history (Yamamoto et al. 2015)

ranging from 25 to 35 MPa at 3 Hz for 5 s. The internal membranes were not damaged but a bleeding was observed at the focal point in 2 mm depth.

10.5 Applications of Numerical Simulation to Clinical Purposes

Those who have unstable aneurysms that may rupture anytime would need immediate treatments. On the other hand, stable aneurysms do not need to have urgent treatments. However, it is not easy to determine the urgent treatment simply by observation of images of the aneurysms. Then neuro-brain surgeons requested numerical analysts whether or not the blood circulations in a three-dimensional

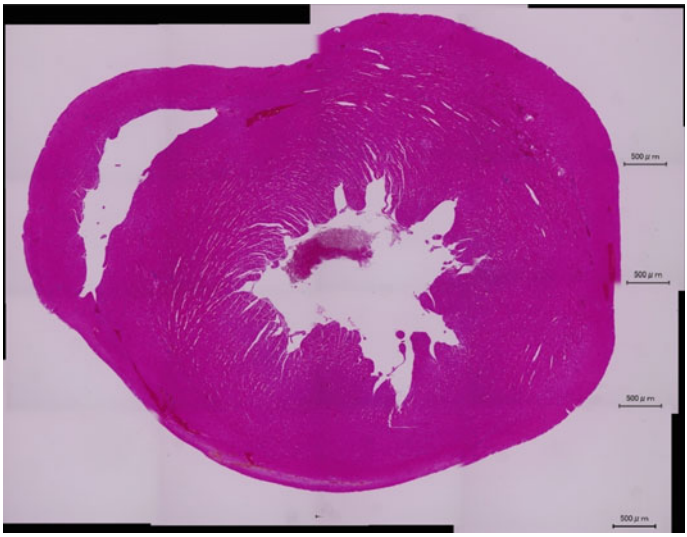

Fig. 10.43 Shock wave focusing on rat's heart. Overpressure at the focal point ranges from 25 to 35 MP (Yamamoto et al. 2015)

replica of patients' aneurysms are possible. In 2000 a project started constructing three-dimensional meshes out of the X-ray images or CT scan images of blood vessels in brains viewed from various directions. At first a software was developed for constructing three-dimensionally distributed blood vessels. Figure 10.44a shows three-dimensional meshes of the blood vessel having an aneurysm in the central part given. At first, the wall boundary of the blood vessel was a solid boundary. At that time, reliable physical properties of aneurysms and living brain blood vessels were not known and hence the simulation was just to examine a blood circulation through complexly shaped three-dimensional pipe line. Elastic deformation was ignored but the Navier-Stokes Equations were solved at non-slip boundary condition. Blood pressures were given according to empirical data. Simulations were conducted, corresponding to various clinical conditions, such as blood pressures and blood mass flow. Figure 10.44b shows one of the primary results. A three-dimensional velocity distribution in blood vessel and an aneurysm. A region with red color indicates blood flow is faster than a region with blue color. Hence in the red color region, the wall shear force is larger than the blue color region. The blood vessel expressed with red color has a higher risk to rupture. Therefore, the numerical simulation would help decision making. However, the result presented in Fig. 10.44 is a preliminary study and many parts should be refined in the near future.

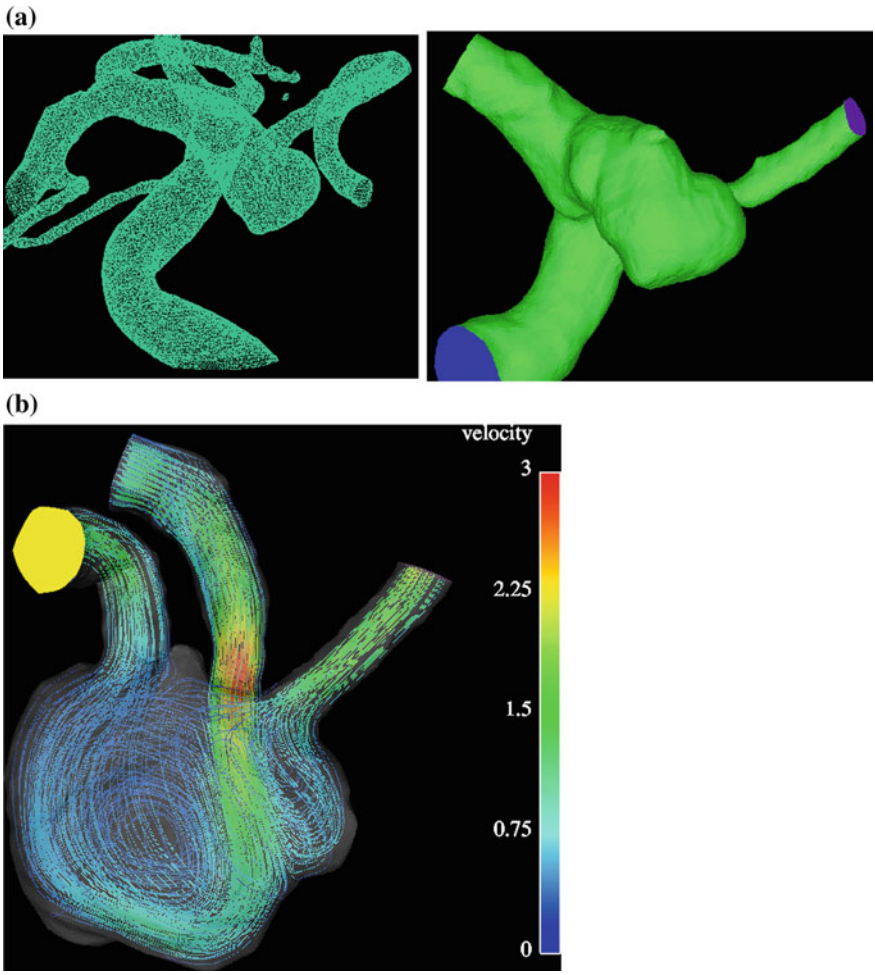

Fig. 10.44 Computational blood flow: **a** computational replica of aneurysm; **b** velocity distribution inside an aneurysm (Hassan et al. 2004)

When the three-dimensional meshes are constructed, we simulated assuming the laminar boundary layer and then imposing appropriate input and outlet flow conditions at the ends of individual blood vessels.

References

Abe, Y., Ise, H., Kitayama, O., Usui, R., Suzuki, N., Matsuno, M., et al. (1990). Disintegration of gallbladder stones by ESWL. *Gallstone, 4,* 451–459.

Bellhouse, H. J., Quikan, N. J., & Ainsworth, R. W. (1997). Needle-less delivery of drugs, in dry powder form, using shock waves and supersonic gas flow. In A. F. P. Houwing, & A. Paul, (Eds.) Proc. 21st ISSW, (Vol. 1, pp. 51–56). Australia: The Great Keppel Island.

Chaussey, C. H., Schmiedt, E., Jocham, D., Walter, V., Brendel, W., Forsmann, B., et al. (1982). *Extracorporeal shock wave lithotripsy. New aspects in the treatment of kidney stone disease*. Muenchen: Karger.

Chaussey, C. H., Schmidt, J. E., Joachim, D., Ferbes, G., Brundel, W., Forsmann, B., et al. (1986). *Extracorporeal shock wave lithotripsy*. Muenchen: Karger.

Hassan, M., Ezura, M., Timfeev, E. V., Tominaga, T., Saito, T., Takahashi, A., et al. (2004). Computational simulation of therapeutic parent artery occlusion to treat giant vertebrobasilor aneurysm. *AINR American Journal of Neuroradiology, 25,* 63–68.

Hirano, T. (2001). *Development of revascularization of cerebral thrombosis using laser induced liquid jets* (MD thesis). Graduate School of Medicine, Tohoku University.

Hirano, T., Uenohara, H., Nakagawa, A., Sato, S., Takahashi, A., Takayama, K., & Yoshimoto, T. (2002). A novel drug delivery system with Ho:YAG laser induced liquid jet. In *Proceedings of the International Federation for Medical and Biological Engineering. 2nd European Conference* (pp. 1006–1007).

Ikeda, K., Matsuda, M., Tomita, K., & Takayama, K. (1999). Application of extracorporeal shock wave on bone. Basic and clinical study. In G. J. Ball, R. Hillier & G. T. Robertz (Eds.), *Shock Waves. Proceedings of 22nd ISSW, London* (Vol. 1, pp. 623–626).

Kambe, K., Kuwahara, M., Kurosu, S., Orikasa, S., & Takayama, K. (1986). Underwater shock wave focusing, an application to extracorporeal lithotripsy. In D. Bershader & R. Hanson (Eds.), *Shock Waves and Shock Tubes, Proceedings of the 15th International Symposium on Shock Waves and Shock Tubes, Berkeley* (pp. 641–647).

Kato, K. (2004). *Study of mechanism and damage threshold of brain nerve cells by shock wave loading* (MD thesis). Graduate School of Medicine, Tohoku University.

Krehl, P. O. K. (2009). *History of shock waves, explosions and impact*. Berlin: Springer.

Kuwahara, M., Kambe, K., Kurosu, S., Orikasa, S., & Takayama, K. (1986). Extracorporeal stone disintegration using chemical explosive pellets as an energy source of underwater shock waves. *The Journal of Urology, 133,* 814–817.

Kuwahara, M., Ioritani, M., Kambe, K., Shirau, S., Taguchi, K., Sitoh, S., et al. (1989). Hyperechoic region induced by focused shock waves in vivo in vitro possibility of acoustic cavitation. *Journal of Lithotripsy and Stone Disease, 1,* 282–287.

Loske, A. M. (2007). *Shock wave physics for urologists*. Universidad National Autonoma de Mexico.

Menezes, V., Takayama, K., Gojani, A., & Hosseini, S. H. R. (2008). Shock wave driven micro-particles for pharmaceutical applications. *Shock Waves, 18,* 393–400.

Nakada. M., Menezes, V., Kanno, A., Hosseini, S. H. R., & Takayama, K. (2008). Shock wave based biolistic device for DNA and drug delivery. *Japanese Journal of Applied Physics, 47*, 1522–1526.

Nagayasu, N. (2002). *Study of shock waves generated by micro explosion and their applications* (Ph.D. thesis). Graduate School of Engineering, Faculty of Engineering, Tohoku University.

Nakagawa, A. (1998). *Basic study of shock wave assisted therapeutic devises in the field of neuro brain surgery* (MD thesis). Graduate School of Medicine, Tohoku University.

Nakagawa, A., Kumabe, T., Kanamori, M., Saito, R., Hirano, T., Takayama, K., et al. (2008). Clinical application of pulsed laser-induced liquid jet: Preliminary report in glioma surgery. *Neurological Surgery, 36,* 1005–1010.

Obara, T. (2001). *A study of applications of underwater shock waves to medicine* (Ph.D. thesis). Graduate School of Engineering, Faculty of Engineering Tohoku University.

Ohki, T. (1999). *Study of medical applications of pulsed Ho:YAG laser induced underwater* (Master thesis). Graduate School of Engineering, Faculty of Engineering Tohoku University.

Okazaki, K. (1989). Fundamental study in extracorporeal shock wave lithotripsy using piezoceramics. *Japanese Journal of Applied Physics, 28,* 143–145.

Shitamori, K. (1990). *Study of propagation and focusing of underwater shock focusing* (Master thesis). Graduate School of Tohoku University Faculty of Engineering, Tohoku University.

Yamamoto, H., Hasebe, Y., Kondo, M., Fukuda, K., Takayama, K., & Shimokawa, H. (2015). Development of a novel shock wave catheter ablation system. In R. Bonazza & D. Ranjan (Eds.), *Shock Waves, Proceedings of the 29th ISSW, Madison* (Vol. 2, pp. 855–860).

Yutkin, L. A. (1950). *Apparat YRAT-1 Medeport USSR Moscow*.